Fast-twitch myofibrils grow in proportion to Mylpf dosage in the zebrafish embryo

Authors:
Tayo E Adekeye – School of Biology and Ecology, the University of Maine, 04469, USA
Emily M Teets – Molecular Genetics, The Ohio State University, 43210, USA
Emily A Tomak – School of Biology and Ecology, the University of Maine, 04469, USA
Sadie L Waterman – School of Biology and Ecology, the University of Maine, 04469, USA
Kailee A Sprague – School of Biology and Ecology, the University of Maine, 04469, USA
Angelina White – School of Biology and Ecology, the University of Maine, 04469, USA
Maddison L Coffin – School of Biology and Ecology, the University of Maine, 04469, USA
Sabrina M Varga – School of Biology and Ecology, the University of Maine, 04469, USA
Teresa E Easterbrooks – School of Biology and Ecology, the University of Maine, 04469, USA
Sarah J Shepherd – Molecular Genetics, The Ohio State University, 43210, USA
Jared D Austin – School of Biology and Ecology, the University of Maine, 04469, USA
Dmitrii Krivorotko – School of Biology and Ecology, the University of Maine, 04469, USA
Troy E Hupper – School of Biology and Ecology, the University of Maine, 04469, USA
Joshua B Kelley – Molecular and Biomedical Sciences, the University of Maine, 04469, USA
Sharon L Amacher – Departments of Molecular Genetics and Biological Chemistry and Pharmacology, The Ohio State University, 43210, USA
* Jared C Talbot – School of Biology and Ecology, the University of Maine, 04469, USA

* Corresponding author
Phone: 207-581-2835
Email: jared.talbot@maine.edu

Abstract

Muscle cells become stronger by expanding myofibrils, the chains of sarcomeres that produce contraction. Here we investigate how Mylpf (Myosin Light Chain Phosphorylatable Fast) abundance impacts myofibril assembly in fast-twitch muscle. The two zebrafish Mylpf genes (*mylpfa* and *mylpfb*) are exclusively expressed in fast-twitch muscle. We show that these cells initially produce six times more *mylpfa* mRNA and protein than *mylpfb*. The combined Mylpf protein dosage is necessary for and proportionate to fast-twitch myofibril growth in the embryo. Fast-twitch myofibrils are severely reduced in the *mylpfa*$^{-/-}$ mutant, leading to loss of high-speed movement; however, by persistent slow movement this mutant swims as far through time as its wild-type sibling. Although the *mylpfb*$^{-/-}$ mutant has normal myofibrils, myofibril formation fails entirely in the *mylpfa*$^{-/-}$*;mylpfb*$^{-/-}$ double mutant, indicating that the two genes are collectively essential to myofibril formation. Fast-twitch myofibril width is restored in the *mylpfa*$^{-/-}$ mutant by transgenic expression of *mylpfa-GFP, mylpfb-GFP,* and by human *MYLPF-GFP* to a degree corresponding linearly with GFP brightness. This correlate is inverted by expression of *MYLPF* alleles that cause Distal Arthrogryposis, which reduce myofibril size in proportion to protein abundance. These effects indicate that Mylpf dosage controls myofibril growth, impacting embryonic development and lifelong health.

Introduction

The myofibril is the contractile organelle of striated muscle, made of chains of sarcomeres that span the cell's length (Figure 1A). Sarcomeres form on the scale of microns, yet their collective function in myofibrils can impact behavior of the entire organism. Despite the importance of myofibril structure and size to muscle strength, it remains unclear how myofibril growth is regulated. One way to control myofibril growth is to regulate the abundance of its component parts. Overall protein levels ('dosage') are influenced by many factors including a gene's copy number, the amount of steady-state transcript produced by each gene ('mRNA abundance'), the steady-state amount of protein encoded by these genes ('protein abundance'), the activity of each encoded protein, and the protein's localization within a cell. In this study, we investigate how the abundance of one key sarcomeric component, Mylpf, impacts myofibril formation. We find that overall Mylpf dosage is controlled by a combination of gene copy number and mRNA abundance, which together predict protein abundance and myofibril size in the zebrafish embryo.

Initially, myofibril formation growth is directed by actin-rich thin filaments [1–3]. These thin filaments contain F-actin strands bundled with nebulin and linked to actinin-rich Z-disks, producing I-Z-I bodies. The ends of I-Z-I bodies are temporarily connected to one another by non-muscle myosin to form pre-myofibrils, which act as a template for further growth [3–7]. Growth is also facilitated in part by integration of enormous contractile proteins titin and nebulin, which set the sarcomere's length [8]. Once pre-myofibrils have formed, the non-muscle myosin is quickly replaced by contractile myosin heavy chain (MyHC), bundled into double-headed thick filaments. These added thick filaments increase tension across the muscle cell, leading to myofibrillar growth [9–11]. Myofibril size then increases along the muscle cell's narrow axis (the 'width axis'), beginning near the cell membrane and then extending into the central cytoplasm[11]. Growth along the width axis increases the myofibril's cross-sectional area, which predicts muscle strength better than overall muscle size does [14].

The class II MyHC in thick filaments is stabilized close to its force-generating head by a Regulatory Light Chain (RLC) and an Essential Light Chain (ELC) protein [12,13]. These light chains regulate myosin movement and force generation but do not consume ATP nor produce force on their own [12]. Point mutations in the RLCs can reduce myosin step size [14], and outright removal of these light chains *in vitro* causes MyHC aggregation and partially reduces MyHC activity [15,16]. Consistent with this finding, the *Drosophila* RLC mutant lacks skeletal muscle [17]. Similarly, the ELC gene *Myl1* is required for normal myogenesis in chicken, zebrafish, mouse, and human [18–20]. Because the primary effect of these light chains is to regulate and stabilize MyHC, we hypothesize that myosin light chain proteins influence the rate of cytoskeletal organization leading to myofibril growth, independent of cell size regulation.

Mylpf (Myosin Light Chain Phosphorylatable Fast) is a light chain of particular interest because it is the only RLC with prominent expression in embryonic muscle fibers and differentiated fast-twitch skeletal muscle in the mouse [21]. All skeletal muscle fibers are absent from the mouse *Mylpf* knockout at birth, suggesting that in mouse this gene may be required in all embryonic fibers [22]. Muscle loss in the *Mylpf*$^{-/-}$ mutant is so complete that it is unclear what phase of myogenesis is disrupted by the mutation. *MYLPF* function is also critical for human development. Missense alleles in *MYLPF* cause Distal Arthrogryposis (DA), a congenital musculoskeletal disease characterized by inherited distal limb contractures [23]. DA is often caused by mutation in genes that encode contractile proteins [24,25]. However, muscle strength nor structure was not examined in human patients with the MYLPF variants, and the impact of those variants have not been tested in animal models. Therefore, the impact of *MYLPF* missense alleles on muscle remains unresolved.

In vertebrates, muscle formation begins in segments of mesoderm called somites, which eventually produce most of the muscles in the body. Somite development proceeds quickly in zebrafish, leading to formation of two fiber types, fast-twitch and slow-twitch, within the first day post fertilization (dpf) [26]. Whereas slow-twitch fibers

contract and fatigue slowly, the zebrafish fast-twitch fibers contract with such speed and power that they nearly strain muscle cells to the point of snapping [27,28]. In zebrafish, the slow-twitch fibers are specified in the medial edge of the somite, then most of these cells migrate to the lateral surface of the somite adjacent to the ectoderm, leaving behind only a set medial slow muscle at the horizontal myoseptum [26]. By 24 hours post fertilization (hpf), all muscle fibers medial to this thin slow-twitch layer are fast-twitch [26]. These positions are retained through embryonic development, enabling us to identify fiber types by position in addition to molecular markers of fiber type. Muscle fibers grow continuously during embryonic development, more than doubling in size by the time of hatching (3 dpf) [29]. Hatched larvae continue growing while subsisting on their yolk until 6 dpf, enabling study of early larval growth independent of feeding.

In zebrafish, Mylpf gene function is distributed across two paralogs, *mylpfa* and *mylpfb* [30–33]. Each gene has one primary transcript in the University of California Santa Cruz genome browser and in Ensembl (Figure 1B) [34]. The two zebrafish Mylpf proteins are 94% identical to one another and each is 89% identical to human MYLPF in both primary sequence and predicted protein structure (Figure 1C). The *mylpfa* and *mylpfb* frameshifting alleles used in this study are predicted to be functionally null because they truncate proteins within the first of two calcium-binding EF-Hand domains (Figure 1D). We previously showed that zebrafish *mylpfa*$^{-/-}$ mutant animals can form multinucleate muscle cells but have weakened muscle that eventually deteriorates [35]. However, the impact of *mylpfa* on myofibrils remained untested and the requirements for *mylpfb* function in embryonic development remained unexplored.

Here, we investigate the effect of Mylpf activity on myofibril development within the somite. We generated a frameshifting *mylpfb* mutation within the first EF-Hand domain, to mirror published [35] *mylpfa* alleles (Figure 1B-E). This *mylpfb*$^{-/-}$ mutant alone has no overt muscle defect, but the *mylpfb* mutation enhances the *mylpfa*$^{-/-}$ mutant phenotype. Examination of animals heterozygous or homozygous for the two mutations reveals that myofibril widths in loss of function are predicted by wild-type Mylpf dosage. Transgenic expression of *mylpfa* and *mylpfb* efficiently rescues the *mylpfa*$^{-/-}$ mutant when either

gene is expressed at high abundance. A transgene expressing human *MYLPF* also rescues the mutant, suggesting conserved function across vertebrate taxa. By contrast, expression of *MYLPF* alleles thought to cause DA ('DA-causing' alleles) disrupt myofibril formation in the *mylpfa*$^{+/+}$ wild-type zebrafish, with a dominant human allele causing more severe defects than a recessive human allele. Together, these findings suggest that Mylpf activity controls myofibril growth by promoting MyHC localization to the site of myofibril formation during early fast-twitch myogenesis.

Results

mylpfa mRNA and Mylpfa protein are expressed more abundantly than *mylpfb* / Mylpfb during embryonic development

Although *mylpfa* and *mylpfb* expression patterns have been described individually [36], their overlap and relative abundance have not been clarified. Transcripts for both Mylpf genes are restricted to fast-twitch muscle, but the *mylpfb* labeling is dimmer as assessed by Hybridization Chain Reaction based RNA *in situ* hybridization (HCR ISH) (Figure 1F-H, S1). Neither gene is expressed in slow-twitch muscle, which expresses a different regulatory light chain, *myl10* (Figure 1F) [37]. Expression of *mylpfa* and *mylpfb* is seen as early as 20 hpf in medial fast-twitch fibers (Figure S1). At 24 hpf, expression of *mylpfa* is around 6 times greater than *mylpfb* when assessed by HCR ISH. The ratio decreases to 3:1 by 36 hpf, largely because of rising *mylpfb* mRNA abundance (Figure 1G, H). Expression of *mylpfa* remains more abundant than *mylpfb* through embryonic stages (Figure 1G, H). Our HCR ISH finding at 24 hpf is close to the 7 to 1 ratio we find for *mylpfa* and *mylpfb* at 27 hpf in an RNA-seq dataset we previously published (Figure 1I) [38]. To investigate whether transcript levels predict protein abundance, we generated and tested new antibodies that recognize both Mylpfa and Mylpfb, which differ by 2 kilodaltons (kD). The relative protein abundance correlates with transcript levels. For instance, the Mylpfa and Mylpfb proteins are expressed in a 6:1 ratio at 24 hpf and 3:1 at 36 hpf (Figure 1I, J). We confirmed antibody specificity by examining the *mylpfa*$^{-/-}$ mutant embryos at 72 hpf. The mutant lacks the Mylpfa band without any change in the

Mylpfb band intensity (Figure 1K). In summary, the two zebrafish Mylpf genes are expressed in fast-twitch muscle, but Mylpfa is produced more abundantly than Mylpfb.

mylpfa is required for the localization of fast-twitch myofibril components, but not for muscle size

To investigate the possibility that the abundant gene *mylpfa* is required for myofibril structure, we compared F-actin localization in the *mylpfa*$^{-/-}$ mutant to its wild-type sibling at 48 hpf, when the fast-twitch myofibrils have thickened. The *mylpfa*$^{-/-}$ mutants have normal slow-twitch fibers but severely disordered F-actin in fast-twitch muscle (Figure 2A-B', S2). Only a small amount of myofibril forms within the fast-twitch muscle of the *mylpfa*$^{-/-}$ mutant (Figure 2C). This myofibril growth defect reflects a failure to organize subcellular components of the myofibril, not overall muscle growth. For instance, the somite's cross-sectional area is unchanged in the *mylpfa*$^{-/-}$ mutant (Figure 2A'', B'', D). Likewise, western blot indicates that MyHC abundance is unchanged in the *mylpfa*$^{-/-}$ homozygotes, suggesting that there is ample protein production (Figure 2E-E'). Total Mylpf abundance is reduced to 54% because Mylpfa protein is completely lost and there is little compensation by Mylpfb (Figures 1L, 2E-E'). Other myofibril markers are also expressed with wild-type abundance but show impaired organization in the *mylpfa*$^{-/-}$ mutant (Figure 2F-I). The myofibrils are narrower in the mutant, but sarcomere length is unchanged (Figure 2J). Using this constant length, we developed an image analysis protocol that assesses the fraction of protein in an image localized to sarcomere-length objects, which we dub the 'sarcomeric fraction' (Figure S3). The sarcomeric-fraction is reduced by half in the *mylpfa*$^{-/-}$ mutant fast-twitch muscle for all proteins tested, matching the reduction in overall Mylpf protein abundance (Figure 2K-L, S3). We generated a *mylpfa:mylpfa-GFP* Tol2 transgene, which produces Mylpfa-GFP protein at around half the native level (Figure 3A, B). This transgene restores both the sarcomeric fraction and myofibril width in the *mylpfa*$^{-/-}$ mutant (Figure 3C-F). This myofibril restoration persists to at least 6 dpf, though some delocalized GFP is seen at that later time-point (Figure 3G, S4). Together these findings show that *mylpfa* has no impact on overall muscle size but is required for the cytoskeletal organization that leads to myofibril growth.

The *mylpfa*$^{-/-}$ mutant myofibril defect is rescued by *mylpfa-GFP* in a dose-dependent manner

The *mylpfa:mylpfa-GFP* transgene exhibits a wide range of expression levels, due in part to positional effects from transposon insertion[39]. By combining the *mylpfa-GFP* transgene with the *mylpfa*$^{-/-}$ mutant, we can test the correlation between Mylpf dosage and fast-twitch myofibril growth within individual animals. We hypothesized that wild-type animals produce Mylpf protein close to its saturation point, where additional protein does not improve myofibril formation, but that the *mylpfa*$^{-/-}$ mutant produces Mylpf well below this saturation point. Consistent with our prediction for the mutant, we see linear correlation between GFP brightness and myofibril width in the *mylpfa*$^{-/-}$ mutant (Figure 3G). Consistent with our prediction for wild-type, we find a slight upward trend, but no significant increase, in myofibril width in wild-type animals that express the *mylpfa-GFP* transgene (Figure 3G). To confirm that myofibril size correlates with GFP brightness, we also examined somite muscle in cross-section and used image thresholding to quantify the myofibril cross-sectional area within the somite (Figure 3H-K). As expected, the overall muscle cross-sectional area does not change in the *mylpfa*$^{-/-}$ mutant or in transgenic animals, because *mylpfa* is required to localize proteins within muscle, not for muscle growth (Figure 3H). Also as predicted, the cross-sectional area of myofibrils is reduced in the *mylpfa*$^{-/-}$ mutant and restored by the *mylpfa-GFP* transgene to a degree linearly correlated with GFP brightness (Figure 3I-M). Together these findings suggest that Mylpfa expression restores the *mylpfa*$^{-/-}$ mutant proportionate with dosage, but added Mylpfa has little impact on the wild-type animal.

Expression of *mylpfb* restores myofibril formation in the *mylpfa*$^{-/-}$ mutant

The differential requirement for *mylpfa* versus *mylpfb* in myofibril formation could be explained either by differences in expression levels or coding sequence. To test the efficiency of *mylpfb* in promoting myofibril growth, we generated a transgenic construct that expresses *mylpfb-GFP* under the *mylpfa* promoter, *tg(mylpfa:mylpfb-GFP)*. The *mylpfb-GFP* fusion protein localizes to the A-band of the wild-type myofibril and enables F-actin to localize in sarcomeric repeats efficiently in the *mylpfa*$^{-/-}$ mutant; similar

localization is seen in animals mosaic for the *mylpfa-GFP* construct (Figure 4A-E). Both constructs have a similar ability to restore myofibril structure in the *mylpfa*$^{-/-}$ mutant (Figure 4F). The average localization of GFP to the myofibril is lower for Mylpfb-GFP compared to Mylpfa-GFP, but the difference is not statistically significant (Figure 4F). The Mylpfb-GFP brightness correlates linearly with myofibril width, with a slope similar to Mylpfa-GFP (Figure 4G). To confirm these mosaic findings, we established germline-inherited transgenic lines for *tg(mylpfa:mylpfa-GFP)mai102* and *tg(mylpfa:mylpfb-GFP)mai103*. Both constructs rescue the *mylpfa*$^{-/-}$ mutant with similar trendlines, though the *mylpfb-GFP* transgene has lower peak brightness than the *mylpfa-GFP* transgene (Figure 4H). These findings support our hypothesis that the two zebrafish Mylpf genes differ primarily by their expression levels.

Early protein abundance correlates with *mylpfa* and *mylpfb* gene requirements in fast-twitch myofibrils

To further investigate how Mylpf gene dosage influences myofibril size, we examined somite muscle structure in both homozygote and heterozygote offspring of the *mylpfa*$^{+/-}$*;mylpfb*$^{+/-}$ heterozygous incross at 48 hpf. As expected, slow-twitch muscle structure is normal across the *mylpfa* and *mylpfb* mutant combinations at this stage (Figure 5A-D). Myofibrils are normal in the *mylpfb*$^{-/-}$ mutant fast-twitch muscle, severely defective in the *mylpfa*$^{-/-}$ mutant, and completely lost in the *mylpfa*$^{-/-}$*;mylpfb*$^{-/-}$ double mutant (Figure 5E-J). In the double mutant, both F-actin and MyHC are scattered throughout the cytoplasm of the fast-twitch muscle cell, suggesting that even the pre-myofibrils may eventually break down in this genotype (Figures 5H', S5). To investigate how well these phenotypes map to Mylpf dosage, we plotted the correlation between myofibril width and the Mylpf dosage, calculated by number of alleles skewed 6:1 for the relative protein abundance at 1 dpf. We find a linear relationship between myofibril width and predicted Mylpf dosage between the *mylpfa*$^{-/-}$*;mylpfb*$^{-/-}$ double mutant (0% dose) and the *mylpfa*$^{+/-}$*;mylpfb*$^{+/-}$ double heterozygote (50% dose), with lessening effect at higher dose (Figure 5J). Consistent with dose-dependent function, the *mylpfa*$^{+/-}$*;mylpfb*$^{+/-}$ double heterozygote shows modestly reduced myofibril width in fast-twitch muscle fibers at 48 hpf (Figure 5I, J orange). The *mylpfa*$^{-/-}$*;mylpfb*$^{+/-}$ homozygote-heterozygote

combination has a sarcomere defect indistinguishable from the doubly homozygous mutant, *mylpfa*$^{-/-}$;*mylpfb*$^{-/-}$ (Figure 5I, J green) suggesting a minimal threshold of Mylpf dosage is needed for any myofibril assembly. We find similar trends by calculating the sarcomeric fraction of MyHC and F-actin in these 48 hpf images (Figure 5K, S5). The correlates persist at 72 hpf, suggesting that the dose effects are constant through embryonic development (Figure 5L, M). Further support for sarcomere loss is seen using TEM at 72 hpf, where the *mylpfa*$^{-/-}$;*mylpfb*$^{-/-}$ double mutant fast-twitch muscle shows only a scattering of thick filaments and I-Z-I bodies and no myofibrils (Figure 5N-P). Quantification of TEM images at 72 hpf is consistent with findings from immunofluorescence (Figure S5). Together with our expression analysis, these findings suggest that the Mylpf expression levels at 1 dpf predict the extent of myofibril formation in somite muscle at 2 and 3 dpf.

mylpfa and mylpfb **are essential to MyHC localization, but not F-actin localization, during early myofibril growth**

Our analysis at 2 and 3 dpf revealed that Mylpf function is required for myofibril structure, but did not clarify which step of myofibril formation is regulated by Mylpf. We hypothesized that sarcomeres may be disordered in the *mylpfa*$^{-/-}$ mutant because of an initial defect in MyHC localization, independent of initial F-actin ordering. We examined the *mylpfa*$^{+/-}$;*mylpfb*$^{+/-}$ heterozygous incross at a stage (26 hpf) when fast-twitch myofibrils have recently begun to thicken. Wild-type and *mylpfb*$^{-/-}$ mutant siblings have normal myofibrils at this early stage, (Figure 6A-B'), consistent with the low abundance of *mylpfb* at 24 hpf. However, the *mylpfa*$^{-/-}$ mutant fails to properly localize MyHC to the fast-twitch muscle cell's periphery where pre-myofibrils are forming (Figure 6C-C'). The localization defect is even more severe in the *mylpfa*$^{-/-}$;*mylpfb*$^{-/-}$ double mutant, suggesting that *mylpfb* also contributes to early myofibril formation (Figure 6D-D'). Since myofibrils normally form at cell peripheries, we assessed localization by quantifying how far the F-actin and MyHC labels spread into the central cytoplasm of fast-twitch muscle cells (Figure 6E). As expected, F-actin and myonuclei are positioned normally within the cell in all genotypes examined (Figure 6F, G), consistent with models that actin localization precedes thick filament localization [5]. MyHC is also localized at cell

peripheries in the wild-type embryo, but MyHC spreads evenly through the cytoplasm of the *mylpfa*$^{-/-}$;*mylpfb*$^{-/-}$ double mutant (Figure 6H). Similarly, the sarcomeric fraction shows a severe MyHC defect but only a subtle change in F-actin localization in the *mylpfa*$^{-/-}$;*mylpfb*$^{-/-}$ double mutant at 26 hpf (Figure S5). These findings suggest that Mylpfa and Mylpfb together are essential to localize MyHC to the fast muscle cell's periphery where the thick filaments interdigitate with pre-myofibrils to initiate myofibril growth.

The zebrafish larva compensates for impaired fast-twitch myofibrils by moving slowly more often

Zebrafish movement is driven largely by force generated in somite muscle [27]. The zebrafish *mylpfa;mylpfb* knockout series allows us to investigate how fast-twitch myofibril growth impacts swimming behavior. Our prior work showed that *mylpfa* is essential to muscle strength and fish movement, leading to a severely impaired escape response[35]. In further support, high-speed imaging shows that the sharp flexure driving initial escape response (the 'C-bend') is consistently absent from this mutant (Figure 7A-C, Video 1). To investigate whether these bursts of escape behavior are mirrored by overall movements, we assayed overall behaviors for 25-minute sessions using DanioVision, across the nine combinations of *mylpfa* and *mylpfb* zygosity at 6 dpf (Figure 7D-I). Consistent with the escape response defect, we find that the highest speed of movement is reduced in all animals homozygous for *mylpfa*$^{-/-}$, which do not swim faster than 70 mm/sec (Figure 7D, E). However, we were surprised to find that the overall speed is not decreased in any of the *mylpfa*;*mylpfb* mutant combinations, which travel at least as far as wild-type siblings during the imaging period (Figure 7F, G). The *mylpfa*$^{-/-}$ mutant animals maintain a high average speed by increasing their frequency of movement at slow speeds, 20-40 mm/sec (Figure 7H). These 6 dpf fish spend most of their time stationary (Figure 7I), consistent with previous findings [40]. When they do swim, the animals move slowly over 99% of the time, so even a slight increase in the likelihood of slow movements can outpace the complete loss of high-speed movement (Figure 7I, J). Both slow and fast movements increase in heterozygous combinations, such as the *mylpfa*$^{+/-}$;*mylpfb*$^{+/-}$ double heterozygote, which on average swims a little

further than its wild-type sibling (Figure 7F-J). The compensatory movement in the *mylpfa*$^{-/-}$ mutant may cause or result from hypertrophy of slow-twitch myofibers (Figure 7K-M). Together these findings suggest that fast-twitch muscle function is only required for the swiftest movements and that slower movements increase when the fast-twitch muscle is compromised.

Myofibril structure is disrupted by the expression of disease-causing MYLPF alleles

Missense alleles of human MYLPF cause DA [35], but it remains unclear how these alleles impact myofibril formation. We hypothesize that these alleles may be antimorphic, inverting the correlations between dosage and myofibril width. We tested the functional impact of the DA-causing variants using plasmids that encode GFP-tagged MYLPF protein variants, driven by the *mylpfa* promoter (Figure 8). We made three plasmids with different MYLPF alleles: the typical allele ('WT'), a dominant allele encoding p.Gly163Ser ('G163S'), which affects a residue that directly contacts MyHC, and a recessive allele encoding p.Cys157Phe ('C157F') that affects a residue buried within the MYLPF protein (Figure 8A) [35]. When expressed brightly, the WT *MYLPF-GFP* allele restores myofibril formation in the *mylpfa*$^{-/-}$ mutant, indicating that function is conserved between zebrafish and human (Figure 8B-D). Mosaic expression of the C157F *MYLPF-GFP* mildly reduces myofibril width in wild-type fish but can partially rescue width in the *mylpfa*$^{-/-}$ mutant, suggesting that it has reduced activity and a slight antimorphic effect (Figure 8B, E, F). The G163S *MYLPF-GFP* allele cannot rescue the *mylpfa*$^{-/-}$ homozygote at 48 hpf and partially narrows myofibrils in the wild-type siblings (Figure 8B, G, H), suggesting that it has no positive function and some antimorphic activity. The G163S variant is mildly detrimental to both wild-type and mutant myofibrils, with increasing effect at high dosage (Figure 8I). In all cases, the shifts in myofibril width correlate well with GFP brightness, such that in the *mylpfa*$^{-/-}$ mutant WT MYLPF-GFP increases width, the C157F allele does so less efficiently (Figure 8I). The activity of these DA-causing alleles in zebrafish is consistent with their inheritance in humans since the more disruptive variant, G163S, causes DA as a heterozygote while the partially functional variant, C157F, causes DA only when homozygous.

Discussion

The task of linking gene and protein dosage to phenotype is typically complicated by dynamic expression patterns and post-transcriptional regulation. Our experiments suggest that both Mylpf genes in zebrafish behave in a manner predicted by a straightforward interpretation of the central dogma. They each produce a single transcript in a single cell type and their transcriptional levels match their relative protein dosage. Gene copy number alone is a poor predictor of Mylpf knockout phenotype, because animals with very different phenotypes (*mylpfa*$^{-/-}$, *mylpfb*$^{-/-}$, and *mylpfa*$^{+/-}$;*mylpfb*$^{+/-}$) carry two mutant alleles of Mylpf and 50% of the normal wild-type alleles. However, we can accurately predict knockout phenotypes when we scale gene copy number by the relative dosage of Mylpfa and Mylpfb protein 24 hpf (6:1) (Figure 8J). Western blotting suggests there is little genetic compensation by Mylpfb in the *mylpfa*$^{-/-}$ mutant, nor much change in native protein levels when Mylpfa-GFP is expressed. We have not been able to test for the presence of the Mylpfb band in the *mylpfb*$^{-/-}$ mutant which cannot be behaviorally sorted from wild-type siblings. Instead, knockout and transgenic rescue studies suggest that Mylpf dosage and phenotype are co-linear between 0% (*mylpfa*$^{-/-}$;*mylpfb*$^{-/-}$) and 50% (*mylpfa*$^{+/-}$;*mylpfb*$^{+/-}$) of the wild-type dose, with diminishing returns at higher expression. The shape of this response curve suggests that Mylpf function in the wild-type embryo sits near or slightly above the saturation point for protein function. Consistent with wild-type saturation, introduction of an extra gene copy (the *mylpfa:mylpfa-GFP* transgene) causes little or no increase in myofibril width in the *mylpfa*$^{+/+}$ wild-type embryo. When beginning from a lower dose (the *mylpfa*$^{-/-}$ mutant), myofibril width can be restored to a degree linearly correlated with Mylpfa-GFP and Mylpfb-GFP protein abundance. We suggest that the dosage effects may not be limited to zebrafish, because human MYLPF-GFP rescues the *mylpfa*$^{-/-}$ mutant as efficiently as the zebrafish genes do. However, the dosage-phenotype correlate is lessened or reversed when we introduce MYLPF protein variants that cause DA, suggesting that normal activity level is vital to MYLPF protein function (Figure 8I, J). Together, these findings poise the two zebrafish Mylpf genes as excellent models for

383 investigating a direct link from gene copy number and mRNA expression levels to
384 protein dosage and myofibril phenotype in the embryo.
385
386 Our work suggests that Mylpf controls myofibril organelle size without affecting overall
387 cell size. We propose that the cell uses Mylpf dosage to regulate localization of MyHC
388 to cell peripheries, particularly in situations where Mylpf abundance is limiting. These
389 limiting situations arise in the *mylpfa*$^{-/-}$ mutant but may also be present in the wild-type
390 animal during rapid growth. At least three mechanisms could explain the impact of Mylpf
391 on MyHC localization. First, since Mylpf is classically thought to stabilize contractile
392 MyHC, the thick filaments deficient in Mylpf protein may be marked as
393 misfolded/defective, triggering the mis-localization and myofibrillar defects [41]. Second,
394 once incorporated into myofibrils, RLCs continue to have known roles in muscle
395 contraction, such as increasing myosin step size leading to enhanced actin movement
396 [14,42]. Impaired step size is expected to reduce muscle force, which would reduce the
397 tension-driven elements of myofibril growth [7,10]. Third, Mylpf may act on non-contractile
398 myosin to mediate thick filament localization. For instance, RLC proteins are known to
399 bind to *myo18b*, an ATPase-deficient MyHC that stabilizes myosin-actin interactions
400 [13,43]. Consistent with this model, the zebrafish *myo18b*$^{-/-}$ mutant shows myofibril
401 formation defects similar to the *mylpfa*$^{-/-}$ mutant [44,45]. Future work to determine precisely
402 how Mylpf regulates myofibril growth may provide new ways to enhance muscle growth
403 after exercise and/or restore it during disease, without requiring cellular hypertrophy.
404
405 The DA gene variants may have antimorphic effects on muscle. The C157F DA allele is
406 recessively inherited in humans [35] and only causes a modest loss of function in early
407 zebrafish development. The G163S allele is dominantly inherited in humans [35] and
408 causes severe loss of function in early zebrafish development. Our results suggest that
409 both variants are antimorphic because both alleles decrease myofibril widths in the wild-
410 type embryo, proportionate with protein dosage. Our model is consistent with recent
411 proposals that most DA-causing alleles may have antimorphic effects [25]. Antimorphs
412 can arise by either gain or loss of protein function, as was established initially using
413 actin alleles in *Drosophila* [46]. For example, a DA-causing *MYH3* allele was recently

shown to increase Myosin activity, leading to hypercontraction and disease, in an antimorphic gain-of-function manner [47]. The DA-causing MYLPF alleles may have antimorphic effects through loss of function, by competing with wild-type MYLPF for binding sites in thick filaments. However, the distinction between loss and gain of function is muddled in these animals. Complete loss of Mylpf function leads to complete loss of fast-twitch myofibrils but it also increases slow-twitch muscle size and causes a gain of low-speed movement (Figure 8J, blue text). We have not yet assessed the behavioral impacts of DA-causing alleles, to learn if animal activity is increased or decreased, because the mosaic fish are labeled too sparsely to assess behavioral changes. Subsequent work using stable transgenes may help elucidate why the DA-causing alleles are antimorphic and may also reveal their impact on behavior.

Over 95% of zebrafish somite muscle is fast-twitch at 6 dpf, so we did not expect the *mylpfa*$^{-/-}$;*mylpfb*$^{-/-}$ double mutant zebrafish to move as far through time as their wild-type siblings while using only ~5% of the normal myofibril volume. The zebrafish *mylpfa*$^{-/-}$ mutant behaves as expected on short timescales, producing force that is reduced by 90% in single-twitch assays [35], consistent with severe reduction in myofibrils throughout fast-twitch muscle. Likewise, *mylpfa*$^{-/-}$ mutant fish lack C-bends, and show an impaired escape response consistent with other fast-twitch deficient fish [35,48,49]. However, the same animals generate slow movements more frequently within the course of our 25-minute experimental window, eventually moving as far as their wild-type siblings. Partial loss of Mylpf function could even increase total movement, since the *mylpfa*$^{+/-}$;*mylpfb*$^{+/-}$ double heterozygote tends to move even further than wild-type siblings. Consistent with our findings, another group recently showed that zebrafish lacking fast-twitch acetylcholine receptors upregulate slow-twitch synapses and behaviors by adult stages [48]. However, this slow-twitch compensation has not previously been observed in larvae and we do not know if there is synaptic compensation in Mylpf mutant zebrafish. The behavioral compensation in Mylpf-deficient animals may be purely due to changes in muscle. Over-reliance on slow-twitch fibers may act as a form of exercise, leading to the observed slow-twitch hypertrophy [28], which in turn should strengthen slow-twitch movement. The importance of muscle hypertrophy and neural activity could be resolved

by investigating muscle strength, calcium signaling, and synapse morphology through time in Mylpf mutants.

Collectively, our findings suggest that Mylpf dosage controls myofibril size, with profound effects on muscle structure and function in zebrafish. *Mylpf* mRNA abundance is enriched in the fast-twitch muscle of farmed mammals that have very tender meat, suggesting that it may be a target of selection on farms [50]. These meat quality factors are predicted by point mutations in the Mylpf promoter region [51]. Likewise, the abundance of *Mylpf* mRNA is a hallmark of muscle differentiation and required for this process [52]. Although the mouse *Mylpf*$^{+/-}$ heterozygote does not have muscle impairment after birth, prenatal muscle disorder has not been ruled out [22]. Mylpf gene dosage does impact muscle development in insects since *Drosophila* heterozygous for RLC mutation has impaired myofibril assembly in fast-twitch flight wing muscle [17]. In some cases, increased light chain activity may also promote new myofibril formation. For instance, activation of cardiac myosin light chain kinase is necessary and sufficient to initiate the formation of sarcomeres in cultured heart cells [53]. These findings lead us to propose that Mylpf abundance is a ripe target for heterometric selection, which alters the prevalence of alleles in a population based on how the alleles affect a gene's expression level. Given how widespread this effect seems to be, the sensitivity of myofibril size to Mylpf dosage may have applications in many contexts where myofibril growth is desired, including exercise physiology, farming, and human health.

Acknowledgements

The fish facilities at the University of Maine fish facility and The Ohio State University (OSU) provided excellent animal care. Dr. Joy-El Talbot from Iris Data Solutions developed an ImageJ macro for sarcomere fraction quantification. Dr. April DeLaurier provided feedback in the writing process. Dr. Clarissa Henry generously provided mentorship and resources to the Talbot lab. Dr. Thomas Gallagher and Collin Whitlock facilitated data sharing between OSU and the University of Maine. Paula Monsma and Dr. Sarah Cole supported imaging on the electron and confocal microscopes at The Ohio State University. This project was supported by a University of Maine Institute of Medicine Seed Grant, and NIH grant R15AR081019 to JCT, NIH R15GM140409 to JBK, by NIH grants GM088041 and GM117964 to SLA, and COBRE P20GM144265-01A1 to JBK and JCT.

Materials and Methods

Zebrafish husbandry and established strains

Fish strains were maintained using standard methods [54]. All animal protocols used in this study were approved by the Institutional Animal Care and Use Committees at The Ohio State University (2012A00000113) and the University of Maine (A2022-09-05). Embryo/larval staging followed established metrics [55]. We genotyped the *mylpfa*^{oz30} 20 bp deletion allele [35] using primers (F 5'-TCTCTACAGGCCAGCTGAATG'3', R 5'-ACCCTTCAACTTCTCTCCGAAC'3') that amplify a 116 bp product in wild-type fish and a 96 bp product in the *mylpfa*^{oz30} homozygote. We genotyped the 1 bp *mylpfa*^{oz43} allele [35], using primers 5'- GCTTCATTGCTGTCAGGATAGAG-3' and 5'-ACCCTTCAACTTCTCTCCGAAC-3', followed by digestion with BsmFI restriction enzyme (NEB, New England Biolabs). The enzyme cuts the wild-type amplicon into two products of similar size (184 bp and 185 bp) and the mutant amplicon (368 bp) remains uncut. Homozygotes for both *mylpfa*^{oz30} and *mylpfa*^{oz43} can be consistently sorted from wild-type siblings based on pectoral fin immobility and by a distinctively slowed escape response. The new mutant and transgenic lines generated during this study are described below. Zebrafish lines in this study were maintained on the AB wild-type background.

Construction of *mylpfb*^{oz39}

The *mylpfb*^{oz39} mutation was generated using established CRISPR-Cas9 protocols [56]. One-cell embryos were co-injected with Cas9 mRNA and guide RNA targeting exon 2 (5'- GGAAAACAGTAAAGTTGATG -3'), raised to adulthood, and outcrossed to identify germline-transmitting founders. F1 progeny were screened using High-Resolution Melting Analysis (HRMA) (primers 5'-CCCTCTCTAAAACAAACAGGCTTTC-3' and 5'-GGTAAGTGAAGATTTGGACAACTC-3') to identify founders carrying a CRISPR-induced *mylpfb*^{oz39} lesion which caused a frameshifting 5 bp deletion. Genotyping for *mylpfb*^{oz39} used primers F 5'-GCAACAATGGGTCAGCTAATG-3' and R 5'-

CCCAAAACCAAAAGTATGAG-3', then PCR products were cut with BccI enzyme (NEB) which cleaved the wild-type amplicon into two products (120 bp and 76 bp) while mutant amplicon (191 bp) remained uncut. The lesion was confirmed via Sanger sequencing of homozygotes and the founder was outcrossed for at least two generations after CRISPR injection, before conducting the experiments shown.

Transgene construction

Plasmid and transgenic construction used traditional restriction enzyme based molecular cloning methods. The five plasmids constructed for mosaic analysis in this study are *pMylpfa:mylpfa-GFP*, *pMylpfa:mylpfb-GFP*, *pMylpfa:WT-MYLPF-GFP, pMylpfa:C157F-MYLPF-GFP, and pMylpfa:G163S-MYLPF-GFP.* Briefly, we obtained GeneArt-strings (Invitrogen) of the sequence encoding Mylpfa*,* Mylpfb*,* wild-type human MYLPF*,* MYLPF p.Gly163Ser (G163S)*,* or MYLPF p.Cys157Phe (C157F) proteins. These coding sequences were inserted into a plasmid containing the *mylpfa* promoter flanked by TOL2 sites [36,57,58]; GFP was linked to the 5' end of Mylpf genes, connected via a sequence encoding a short flexible peptide (GGGGSGAT). Plasmid injection was accompanied by co-injection of zebrafish-optimized nuclear transposase ZT2TP [59,60]. For transient analysis, animals with high levels of mosaicism were selected for imaging and all experiments were repeated on at least two independent injection days. Stable transgenic lines were generated for the two zebrafish transgenes, Tg(*pMylpfa:GFP-mylpfa*)*mai102*, and Tg(*pMylpfa:mylpfb-GFP*)*mai103*. For stable transgenic analysis, at least two founders were analyzed per rescue construct.

Immunohistochemistry and HCR ISH

Whole mount immunohistochemistry used established markers and techniques [61]. Briefly, the larvae were fixed in 4% paraformaldehyde and washed in PBST (1X PBS, 0.1% Tween-20) before immunolabel. Embryos older than 1 dpf were gently permeabilized using a brief treatment with 0.001% Proteinase-K, washed repeatedly in PBST, then blocked for at least two hours in 0.5% TritonX, 1X PBS, 2% NSS, 4% NGS;

1% DMSO [61,62]. This is followed by overnight incubation at 4°C with primary antibodies diluted in blocking solution. We used primary antibodies for the myonuclei (1:500, Rbfox1l) [63]; α-Actinin (1:500, A7732, Sigma); Myomesin [1:30, mMac, Developmental Studies Hybridoma Bank (DSHB)] [64], MyHC (1:1000, A4.1025, DSHB) [65], and Mylpf (1:2000, DZ41336, Boster). The following day, larvae were washed 5-6 times over 1 hour in PBST, and then incubated in secondary antibodies for 4 hours at room temperature. Larvae were washed 6-8 times over 2 hours in PBST, mounted with 0.2% agarose then imaged, or kept in PBST at 4°C prior to imaging. F-actin labeling uses Alexa Fluor-conjugated phalloidin (1:50, Thermo Fisher), added in the final two hours of the secondary antibody incubation. HCR ISH procedures use established protocols with probes and amplifiers supplied by Molecular Instruments [66]. The *mylpfa* and *mylpfb* genes are very similar to one another, so nine unique *mylpfa* probes and five unique *mylpfb* probes could be generated, whereas we were able to generate twenty probes to *myl10*. To compare HCR ISH signal intensity, separate fish were labeled with *mylpfa* and *mylpfb* probes, both in the 488 nm excitation channel and then imaged with matched confocal settings. HCR ISH images were quantified in FIJI using brightness analysis within the fast-twitch region.

Antibody production, validation on Western blot

The zebrafish Mylpf antibody was generated by Boster Bio using zebrafish Mylpfa (AA 14 to 167 of NP_571263.1) in complex with a Mylpf-binding region that is found in several MyHC proteins (RRESIYTIQYNIRSFMNVKHWPWMKVYYKIKPL). This mixture was injected into rabbit via three rounds of injection, followed by column purification and Elisa confirmation by Boster Bio. Western blot in the Talbot Lab, showed only one band each for Mylpfa (16 kD) and Mylpfb (18 kD) and no label in the MyHC size (252 kD). For western blotting, animals were raised to the desired stage, sorted by behavioral phenotypes, then pools of 10 (72 hpf) to 40 (24 hpf) animals were homogenized using 0.5 mm zirconium beads (Laboratory Supply Network) in Bolt solution (Invitrogen). The *mylpfa*$^{-/-}$ mutant animals were sorted by behavioral phenotypes and proper separation was confirmed using PCR genotyping. Homogenized samples were run on a 4-20%

gradient acrylamide gel (Bio-Rad) or an "any kD" precast polyacrylamide gel (Bio-Rad). The protein samples were transferred to Polyvinylidene difluoride (PVDF) membranes (Millipore Sigma) followed by blocking solution (5% nonfat dry milk) overnight at 4˚C. Membranes were incubated in primary antibody at room temperature for 1 hour, followed by incubation in secondary antibody for 2 hours. The resulting fluorescence was measured by scanning the blot with the Odyssey Infrared Imager (LICOR). The Mylpfa to Mylpfb ratio was quantified using GelBox software [67] and FIJI [68]. Primary antibodies included mouse polyclonal anti-MyHC (A4.1025, DSHB, 1:1000) to detect MyHC protein while rabbit polyclonal anti-Mylpf (Boster, 1:1000) detected both Mylpfa and Mylpfb protein. The secondary antibodies used are donkey-anti-mouse-800 (1:10000 dilution) and donkey-anti-rabbit-680 (1:10000 dilution).

Protein modeling

Mylpf proteins were modeled in complex with the binding region of Myhz1.3 (zebrafish) or MYH3 (human) using Robetta [69] and then models were visualized using PyMol (Schrödinger).

Confocal imaging

Confocal images in Figure S2 were collected using an inverted Nikon TiE microscope equipped with an Andor Revolution WD spinning disk confocal system. All other confocal images were acquired using a Leica TCS Sp8 confocal microscope and processed with Lightning in LasX software. Myotomes were imaged over the mid yolk tube region of embryos and larvae. Image settings including laser power and gain were equivalent for compared groups and confocal export protocols were standardized for each experiment.

Sarcomeric fraction calculation

To quantify the degree to which muscle proteins localize to sarcomeres, we developed metric for analyzing how much protein analyzes to sarcomeric repeats, which we term

the sarcomeric fraction (Figure S3). This calculation begins by drawing Region of Interest (ROI) lines along the length of a myofiber in ImageJ, measuring ten to thirty ROIs per image. The grayscale intensities are exported from FIJI and the periodicity of these intensities is determined using the 'distance between peaks' function in MATLAB. Peak-to-peak distances per intensity were determined per image, and bootstrap confidence intervals were calculated using variation between images, shown via histogram to represent the Fraction of Peaks/micron (μm). We used distinct bin sets for markers with full-sarcomere (F-actin, Myomesin, Actinin) or half-sarcomere length (MyHC, Mylpf-GFP). Sarcomeric F-actin shows peak signals in the 0.7-1.1 μm range and 1.55-2.3 μm range, reflecting the fact that most F-actin periods are sarcomere length but sometimes a gap can be seen at the M-line. For consistency, we used this same bin set for Myomesin and Actinin (Figure S3). Sarcomeric MyHC and Mylpf-GFP show two peak signals in bins 0.6-1.2 μm and 1.75-2.05 μm (Figure S3), because these proteins are usually subdivided into the two A-Bands, but sometimes blur together to the length of a full sarcomere. The sarcomeric fraction is the ratio of image periodicity within the sarcomeric length bin to the overall periodicity of that marker. Sarcomere fractions were calculated per animal then subjected to further statistical tests using JMP software.

Quantifying protein localization within cells

To quantify protein localization within muscle cells, we first imaged dorsal somites muscle above the mid yolk tube with high Z-resolution (0.5 μm) and exported a reconstructed cross-section through the somite. Then, a mask was drawn manually, circling the borders of each cell. A custom MATLAB script determined image brightness at each pixel, moving from the periphery of the cells to the center. These edge-center distances were scaled to micron lengths, averaged, and bootstrap confidence intervals were calculated across samples of a given genotype. Graphs with confidence intervals were then overlaid for each genotype.

Myofibril width measurements

To measure myofibril width, we drew region of interest (ROI) lines across the narrow axis of the myofibril in FIJI, typically measuring thirty myofibrils per image. For mosaic animals we measured both GFP+ and non-transgenic myofibrils within the same single confocal slice. Images were included only if they contained at least ten GFP+ myofibrils. For stable transgenics lines, we compared measurements from non-transgenic and transgenic siblings. We generated a custom FIJI macro to simplify measurement and compile all measures from a given image. These measurements were averaged per image using MATLAB and the averages were imported into JMP software for statistical analysis.

GFP brightness analysis

Analysis of fluorescent brightness began during imaging, when we ensured that all data meant for comparison was collected with equivalent settings, such as shared laser power. We evaluated the GFP brightness using the mean grayscale value of the GFP channel in FIJI software. For stable transgenic lines, we drew ROI around the full somite at the center of each image, while excluding the superficial slow fibers. In mosaic animals, we drew ROI around each muscle fiber because there was often a high level of variation within a single image. A custom FIJI macro simplified the measurement of the mean grayscale value of each image. Myofibrils are considered non-transgenic if the GFP brightness is <1 (0-255), were and considered transgenic if in the 10-255 range. MATLAB was used to calculate the average of each mean grayscale value per image followed by statistical comparisons in JMP software.

Transmission electron microscopy

For TEM, embryos were raised to 72 hpf, fixed in glutaraldehyde, resin embedded, thin sectioned, and contrasted using Uranyl acetate and Reynold's lead citrate before imaging on a Tecnai 30 G2 TWIN microscope. At least three fish were examined per genotype and multiple sections were imaged per fish. Statistical analysis was performed using only one image per animal to ensure biological independence. Myofibril widths

and sarcomere fraction were determined using TEM images with magnification low enough to examine variation across a half-somite.

Behavioral analysis

For tail curvature assessment, individual larvae were placed in a petri dish and prodded with a piece of fishing line, imaged using a GoPro Hero camera with a mounting ring (H12Pro, Back-Bone) set to 240 frames/sec. The frame with highest curvature was transferred to FIJI and curvature was measured along the length of the trunk using the Kappa plugin[70]. Total curvature was calculated by multiplying average curvature by the length and then converting from Radians to Degrees. For speed analysis, larvae were placed one per well into a 12-well plate with 3 ml of facility water at 6 dpf. Then, they were imaged in a DanioVision system (Noldus) equipped with a magnifier for improved resolution. The plates were incubated at 28˚C in the preheated chamber. The larvae were imaged using the infrared wavelength every 0.33 seconds for a total of 25 minutes, cycling lights off and on every five minutes. Larvae were tracked using EthoVision XT Version 15.0 video tracking software by Noldus. Distance traveled is the sum of distances in this 25-minute time interval. Speed is calculated per 0.33 second time interval and then binned into different speed ranges using Microsoft Excel Histogram function. Speed bins were selected to best show movement dynamics by speed while reducing noise caused by the rarity of movements at the highest speeds. Analysis was limited to velocities under 200 mm/sec because video examination shows that higher-speed measurements are indications of tracking glitches rather than actual zebrafish movement. Shown plots (Figure 7D-J) integrate data collected from the *mylpfb*$^{+/-}$ heterozygous incross, *mylpfa*$^{+/-}$;*mylpfb*$^{+/-}$ double heterozygous incross, and outcrosses of *mylpfa*$^{+/-}$;*mylpfb*$^{+/-}$ to AB. Each set of crosses was replicated at least three times with consistent results across experiments.

Statistical analysis

We begin multiple comparisons using ANOVA and then use Tukey-Kramer's post-hoc comparison of levels. In one case, where values are bounded closely by zero (Figure

7E), the data cannot follow a normal distribution so we used non-parametric Steel-Dwass comparisons. Pairwise comparisons (Figure 2C, D, E', J) use a two-sided Student's T-test and matching results are found with the non-parametric Krustal-Wallis exact test. In all figures, not significant (n.s.) is P>0.1, * P<0.05, ** P<0.01, *** P<0.001. For box plots, the central line is median, the upper bound is the upper quartile, the lower bound is the lower quartile, and whiskers are 1.5x the interquartile range. Each N represents a different animal or in some cases a pool of animals and are listed explicitly in the source data file. For mosaic animals, the N represents the number of animals scored for GFP+ or non-Tg cells, respectively. Repeated measures of the same animal are averaged and included as a single N. Statistical comparison is made either in Jmp Pro 17 software or, for bootstrapped confidence intervals, in MatLab R2023b.

Data availability

The data leading to conclusions in this paper are shown in the main text figures and supplementary figures, with source data provided. We are happy to accommodate requests for additional source files.

Code availability

Code used for data analysis in this manuscript is available upon request and from our GitHub account, https://github.com/MuscleZebrafish/MyofibrilQuant.

Competing Interest Statement

The authors declare that they have no competing interests.

Figures and Legends

Figure 1: The *mylpfa* gene is expressed more abundantly than *mylpfb* in fast-twitch muscle. **(A)** Illustration of a sarcomere and an image of a fast-twitch myofibril at 26 hpf, with MyHC labeled green using A4.1025 and F-actin labeled magenta using phalloidin. **(B)** Illustration of *mylpfa* and *mylpfb* gene structure and the location of frameshifting alleles used in this study. Shown features include the 5' UTR (brown), coding sequence (purple), 3' UTR (gray), and frameshift locations (green arrows). **(C)** Overlay of predicted protein structures generated using Robetta, showing a high degree of expected similarity between zebrafish Mylpfa, Mylpfb, and human MYLPF proteins. **(D)** Illustration of Mylpfa and Mylpfb proteins, with arrowheads marking frameshift locations. **(E)** Chromatogram showing the gRNA target in wild-type sequence (top) and the 5 bp *mylpfb*^{oz39} lesion sequenced from a homozygous mutant (bottom). **(F-F''')** HCR ISH imaged in somites over the mid-yolk tube of a 36 hpf embryo. Shown as a single channel for *mylpfa* (F), *mylpfb* (F') or the slow muscle marker *myl10* (F''), and as a merged image (F'''). **(G)** HCR ISH shows relative expression levels for *mylpfa* and *mylpfb* through embryonic development. **(H)** Box plot showing the brightness of *mylpfa mylpfb* in the HCR ISH images, with *mylpfa*:*mylpfb* ratios shown per time-point. **(I)** FPKM values for *mylpfa* and *mylpfb* at 27 hpf, from a previously reported RNA-seq dataset [38]. **(J)** Ratio of Mylpfa to Mylpfb band intensity in western blot; points represent biological replicates of pooled animals. **(K)** Image of a western blot showing Mylpfb and Mylpfa protein abundance at 24, 36, 48, and 72 hpf. **(L)** Western blot showing Mylpfb and Mylpfa protein in the wild-type and the *mylpfa*$^{-/-}$ mutant which lacks the Mylpfa band. Significance threshold determined by Tukey-Kramer comparison after one-way ANOVA; * P<0.05, ** P<0.01. Scalebar in F is for F-F'''.

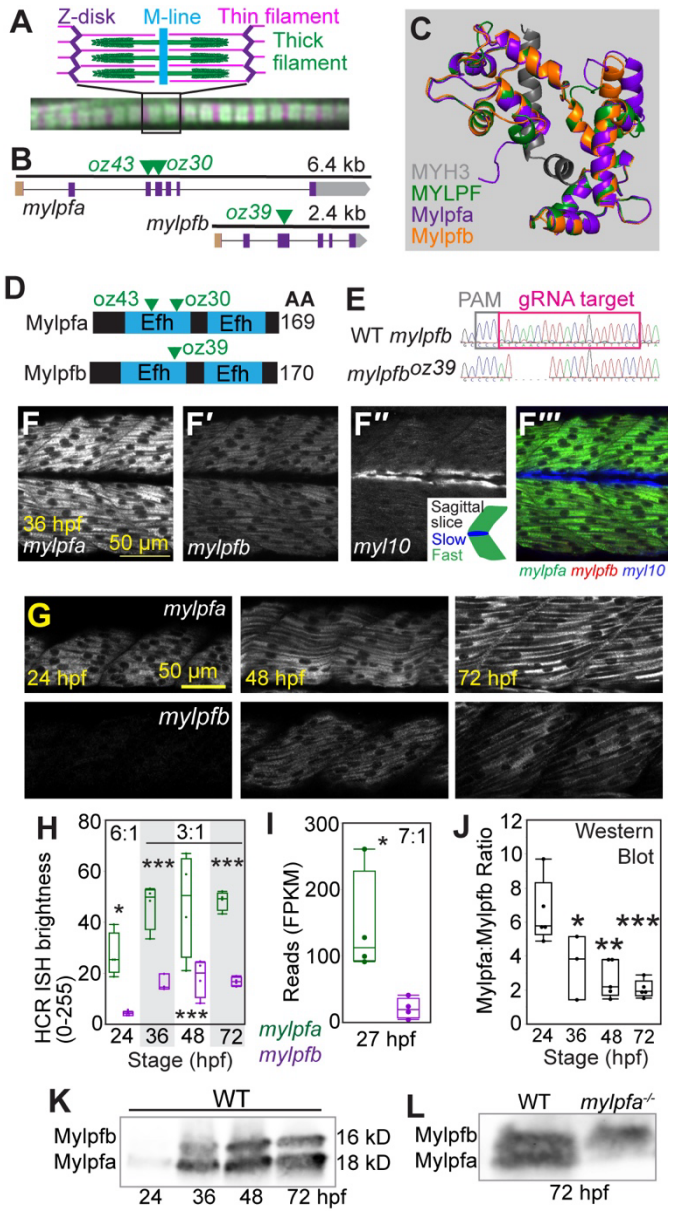

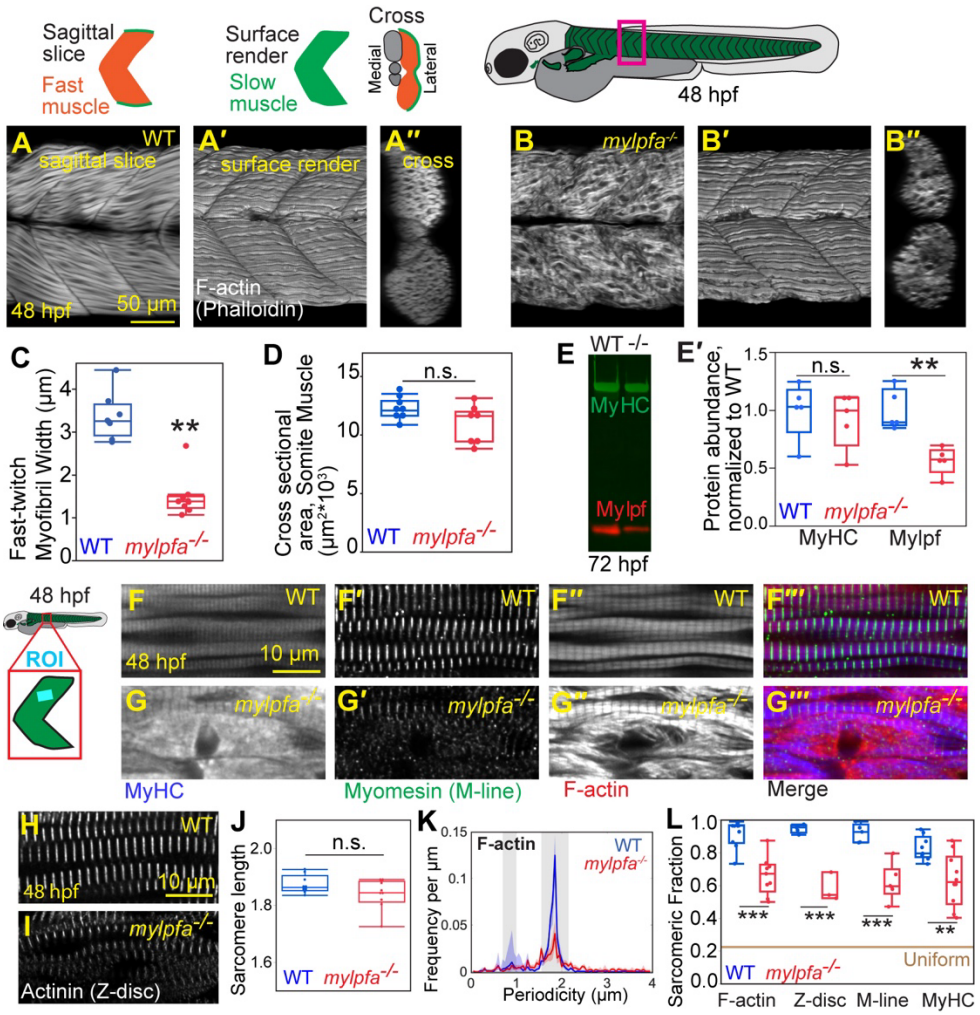

Figure 2: Zebrafish *mylpfa* is necessary for fast-twitch myofibril formation. **(A-B")** Three views of somites are illustrated above (A) and imaged in a wild-type animal and *mylpfa*$^{-/-}$ mutant sibling, each imaged at 48 hpf. **(C)** Box plot of myofibril width, measured from sagittal confocal slices. **(D)** Plot of muscle cross-sectional area (CSA) measured from the orthogonal view of confocal stacks from the wild-type and *mylpfa*$^{-/-}$ mutant siblings. **(E)** Example of a western blot for MyHC and Mylpf, including Mylpfa and Mylpfb, in the wild-type (WT) and the *mylpfa*$^{-/-}$ mutant (-/-) samples at 72 hpf, with **(E')** quantification shown as a box plot. **(F-G''')** Fast muscle myofibers, labeled at 48 hpf, showing co-label for MyHC (A4.1025), M-line (anti-Myomesin), and F-actin (phalloidin), shown as single channel or overlays. **(H, I)** Actinin label on comparable samples. **(J)** Box plot of sarcomere lengths in the *mylpfa*$^{-/-}$ mutant and their wild-type siblings, showing no change in length. **(K)** Plots showing that the *mylpfa*$^{-/-}$ mutant shows reduced F-actin sarcomeric periodicity (gray bars). Lightly colored regions indicate bootstrap confidence intervals. **(L)** Box plot showing sarcomeric fraction for each marker, calculated on a 0-1 scale, as described in Figure S3. Throughout the figures, the wild-type plots are blue and the *mylpfa*$^{-/-}$ plots are red. Points within box plots represent the individual animals or a single western blot image. Scalebar in A is for A-B", in F is for F-G"', in H is for H, I. Significance thresholds for multiple comparisons determined by Tukey-Kramer HSD comparisons after one-way ANOVA; pairwise comparisons use Student's T-test and matching results are found with Krustal-Wallis exact test. Not significant (n.s.) is P>0.1, * P<0.05, ** P<0.01, *** P<0.001.

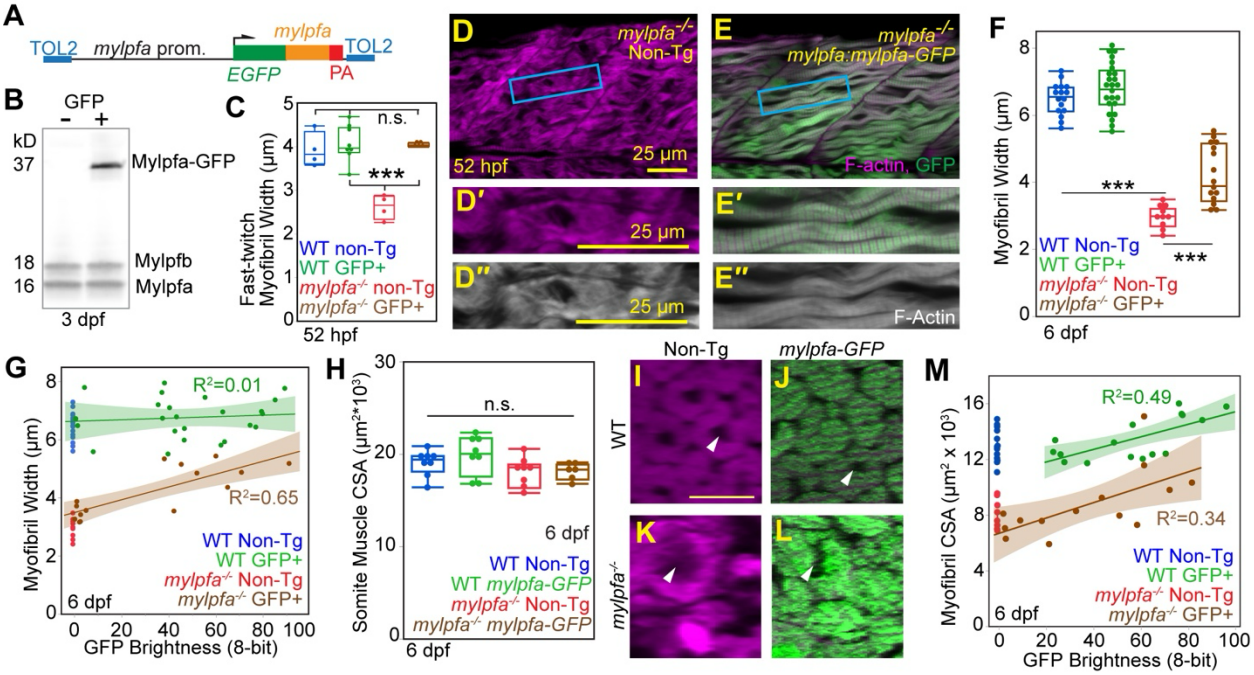

Figure 3: A *mylpfa:mylpfa-GFP* transgene rescues the *mylpfa*$^{-/-}$ mutant. **(A)** Schematic illustrating the *mylpfa:mylpfa-GFP* transgene. **(B)** Western blot of Mylpf protein from the wild-type fish at 3 dpf, and their GFP+ siblings shows that the transgene produces one thin band that is shifted upwards by the addition of GFP. **(C)** Box plot showing the effect of *mylpfa:mylpfa-GFP* transgene expression on the myofibril width at 52 hpf. **(D, E)** Confocal slice through fast-twitch muscle in a non-transgenic (Non-Tg) phalloidin labeled *mylpfa*$^{-/-}$ mutant (D) or a *mylpfa:mylpfa-GFP* transgenic sibling mutant (E) at 52 hpf. **(D', E')** Zoomed view showing myofibril structure. **(D'', E'')** The phalloidin channel showing myofibrils unobscured by GFP. **(F)** Box plot showing myofibril widths in zebrafish at 6 dpf. **(G)** Scatterplot showing correlations between GFP brightness and myofibril width at 6 dpf. **(H)** Box plot of total somite muscle cross-sectional area measurements at 6 dpf, taken from orthogonal views of confocal stacks. **(I-L)** Examples of cross-sectional images, reconstructed from confocal stacks. The myofibril-free central region (Arrowhead) of non-transgenic wild-type muscle (I) is sometimes reduced in the transgenic animal (J). This central area expands in the non-transgenic *mylpfa*$^{-/-}$ mutant (K) but is reduced in the *mylpfa*$^{-/-}$ mutant carrying the transgene (L). **(M)** Scatterplot showing correlations between myofibril cross-sectional area and GFP brightness. Scalebars in D-D''' is for E-E''', in I is for I-L. Significance thresholds are determined by Tukey-Kramer HSD comparisons after one-way ANOVA: ** indicates P<0.01, *** P<0.001, n.s. P>0.1.

Figure 4: Expression of either *mylpfb-GFP* or *mylpfa-GFP* can rescue the *mylpfa*$^{-/-}$ myofibrils. **(A-D)** Images of phalloidin labeled animals at 72 hpf showing mosaic expression of the *mylpfa:mylpfa-GFP* (A, B) or the *mylpfa:mylpfb-GFP* transgene (C, D). **(E)** Box plots showing the fraction of F-actin localized to sarcomeres, calculated in non-transgenic muscle fibers and GFP+ muscle fibers within the same mosaic animals. **(F)** Box plots showing the sarcomeric fraction for GFP. **(G)** Scatterplot showing the correlation between GFP brightness and myofibril width in *mylpfa*$^{-/-}$ mutant animals carrying *mylpfa:mylpfa-GFP* or *mylpfa:mylpfb-GFP* transgenes. Linear correlates for the two transgenes have overlapping confidence intervals. The vertical brown line indicates animals classified as transgenic vs. non-transgenic. **(H)** Scatterplot of myofibril widths in animals bearing an inherited transgene. The Mylpfa-GFP widths in (H) are also presented in Figure 3B, shown here for comparison with Mylpfb-GFP. Scalebar in A applies to A-D. Significance: n.s. is P>0.1, *** indicates P<0.001 as determined by Tukey-Kramer HSD comparisons after one-way ANOVA.

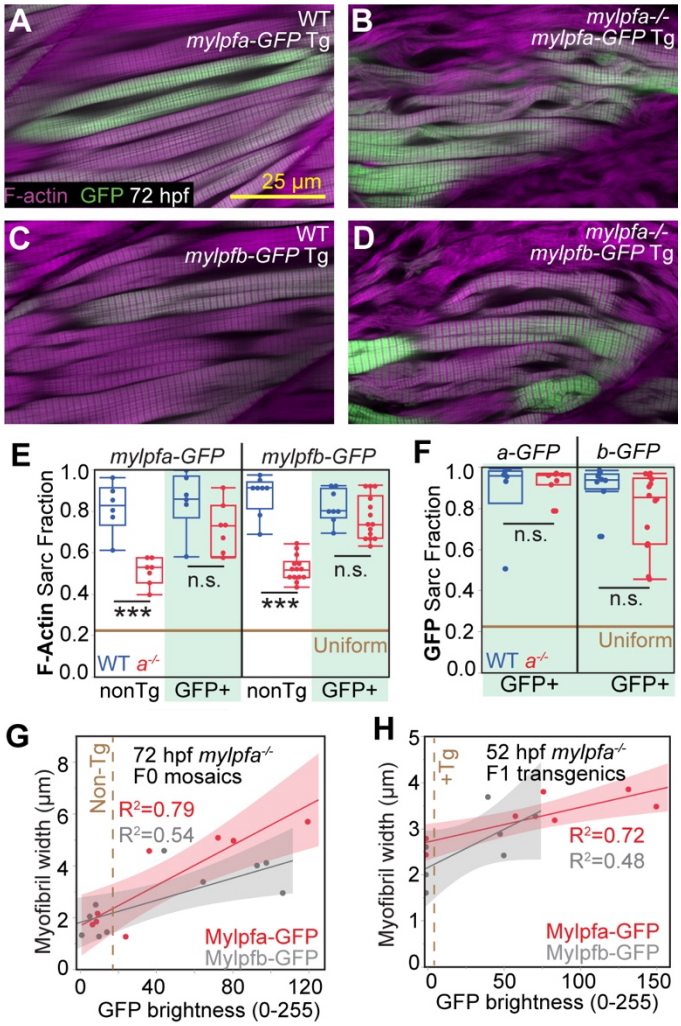

Figure 5: Levels of myofibril formation correspond to dosages predicted by *mylpfa* and *mylpfb* loss of function. **(A-D)** 3D renders of confocal stacks show normal myofibril structure in slow muscle fibers across Mylpf genotype. **(E-H)** Medial slices show a portion of myotome rich in fast-twitch fibers, with robust myofibrils in the wild-type sibling (E) and the *mylpfb*$^{-/-}$ mutant (F), but overt myofibrillar defect in the *mylpfa*$^{-/-}$ mutant (G) and total loss of myofibrils in the *mylpfa*$^{-/-}$;*mylpfb*$^{-/-}$ double mutant (H). Zoomed images show myofibrillar structure within fast-twitch muscle fibers (E'-H'). **(I)** Box plots of myofibril widths in slow-twitch and fast-twitch muscle. Slow and fast-twitch widths plotted separately because the slow-twitch fibers were measured on 3D rendered images and the fast-twitch fibers were measured on confocal slices. **(J)** Scatterplot showing the same myofibril width data from fast-twitch muscle (in I) replotted as a correlate with predicted protein dosage at 24hpf, with each allele scaled 6:1 for Mylpfa:Mylpfb ratio. **(K)** Box plots showing the fraction of sarcomeric MyHC localization. **(L)** Box plots showing myofibril widths in 72 hpf phalloidin-labeled animals. **(M)** Scatterplot of the same data with each allele scaled 6:1 for Mylpfa:Mylpfb. **(N-P)** Transmission electron microscopy showing normal sarcomere structure in the wild-type sibling (N), partial sarcomeric disarray in the *mylpfa*$^{-/-}$ mutant (O) and only scattered sarcomeric components in the *mylpfa*$^{-/-}$;*mylpfb*$^{-/-}$ double mutant (P). Scale bars in D, H, and H' are 10 µm, applicable to their row. Scale bar in N is 1 µm. Significance thresholds: not significant (n.s.) is P>0.1, ** P<0.01, *** P<0.001 as determined by Tukey-Kramer HSD comparisons after one-way ANOVA.

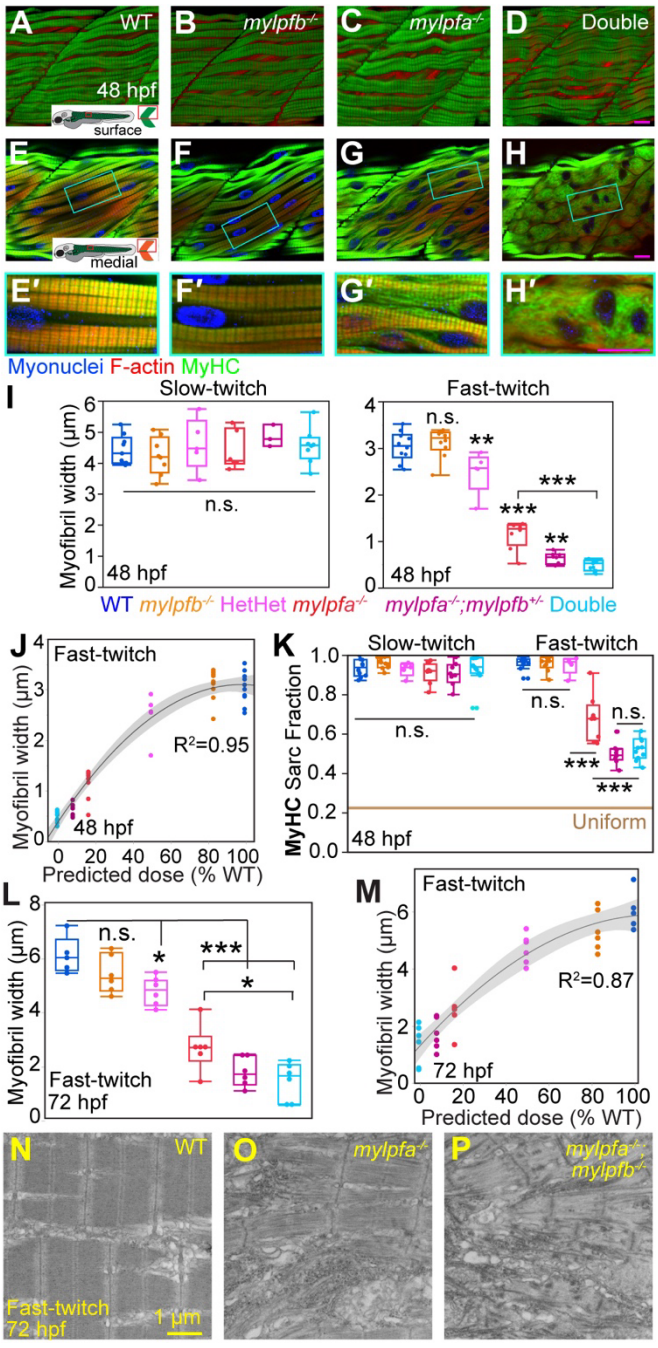

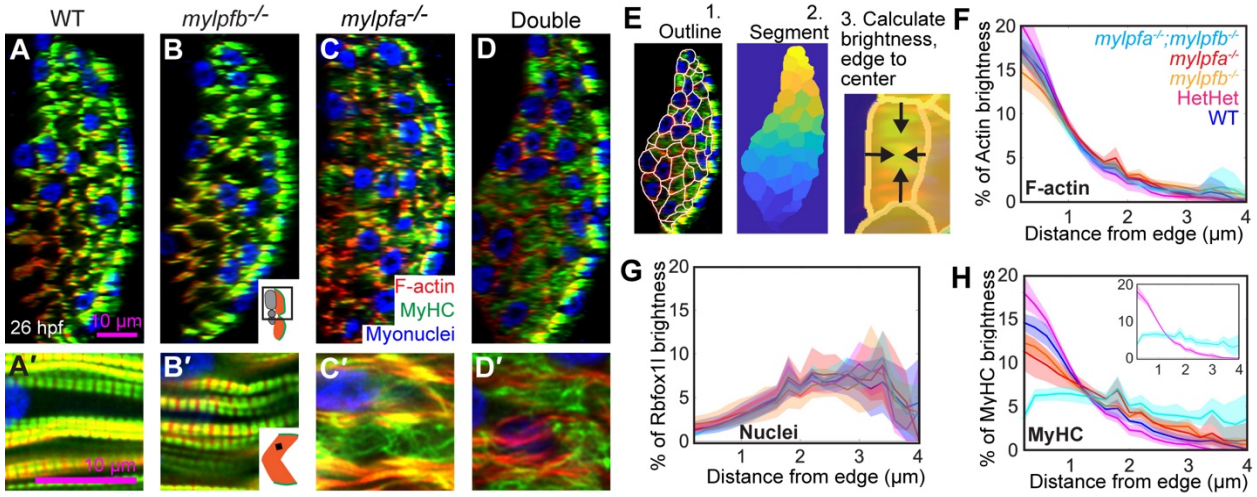

Figure 6: *mylpfa* and *mylpfb* are required for myosin heavy chain localization in young myofibers. **(A-D)** Immunolabel of fast muscle fibers at 26 hpf shown as orthogonal views of Z-stacks of wild-type (A), *mylpfb*$^{-/-}$ (B), *mylpfa*$^{-/-}$ (C), and *mylpfa*$^{-/-}$;*mylpfb*$^{-/-}$ double mutant zebrafish (D). **(A'-D')** Zoomed sagittal views of the same animals. **(E)** Overview of protocol to measure image brightness from edge-to-center. The fast-twitch muscle cells are (1) manually outlined, (2) segmented using these outlines, then (3) label brightness is calculated from edge-to-center of the drawn cells. **(F, G, H)** Localization at 26 hpf of the F-actin marker phalloidin (F), the muscle nuclei label anti-Rbfox1l (G), and MyHC antibody A4.1025 (H). Data is plotted as percent of total image brightness from edge to center of segments, with bootstrapped 95% confidence intervals in shaded lines. F-H uses the genotypic color code shown in (F). Inset in H shows the stark difference between MyHC localization in the *mylpfa*$^{+/-}$;*mylpfb*$^{+/-}$ double heterozygote and the *mylpfa*$^{-/-}$;*mylpfb*$^{-/-}$ double mutant, unobscured by other genotypes. Scalebar in A is for A-D; A' is for A'-D'.

Figure 7: The *mylpfa*$^{-/-}$ and the *mylpfa*$^{-/-}$;*mylpfb*$^{-/-}$ double mutant animals do not swim at high speed but increase the frequency of slower movements. **(A-C)** Escape response in wild-type or in *mylpfa*$^{-/-}$ animals, showing images captured 1/60th of a second apart (A, B). Blue line shows maximal tail bend, quantified in (C). **(D-H)** Box plots of behaviors in a 25-minute interval, imaged using DanioVision. Genotypic color code is shown in (D), with gene names simplified to '*a*' (*mylpfa*) or '*b*' (*mylpfb*). Behavioral analysis incudes the highest speed movement in the interval (D), the percent of time spent swimming swiftly (E), the average speed (F) the distance traveled (G), and the percent of time swimming at slow speed (H). **(I)** A logarithmic plot of the proportion of time that select genotypes swim at different speeds, with bootstrap confidence intervals shown for each genotype. **(J)** The same data is shown after normalization to wild-type behaviors, plotted on a linear scale. **(K, L)** Phalloidin label in the wild-type larva (K) or the *mylpfa*$^{-/-}$ mutant (L), annotated to show the boundary between slow-twitch and fast-twitch muscle fibers at 6 dpf. **(M)** Box plot shows that slow-twitch myofibril CSA is increased in the *mylpfa*$^{-/-}$ mutant and reduced in the mutant by expression of *the mylpfa:mylpfa-GFP* transgene. Data in (K-M) comes from the dataset examined in Figure 3H-M for other measures. Scalebar in A is for A-B, in K is for K-L. Significance is determined using Tukey-Kramer comparisons after one-way ANOVA, shown as n.s. of P>0.1, * P<0.01, ** P<0.01 and *** P<0.001 in these comparisons. For comparison between groups bounded by zero, we used non-parametric Steel-Dwass comparisons (~~~ P<0.001).

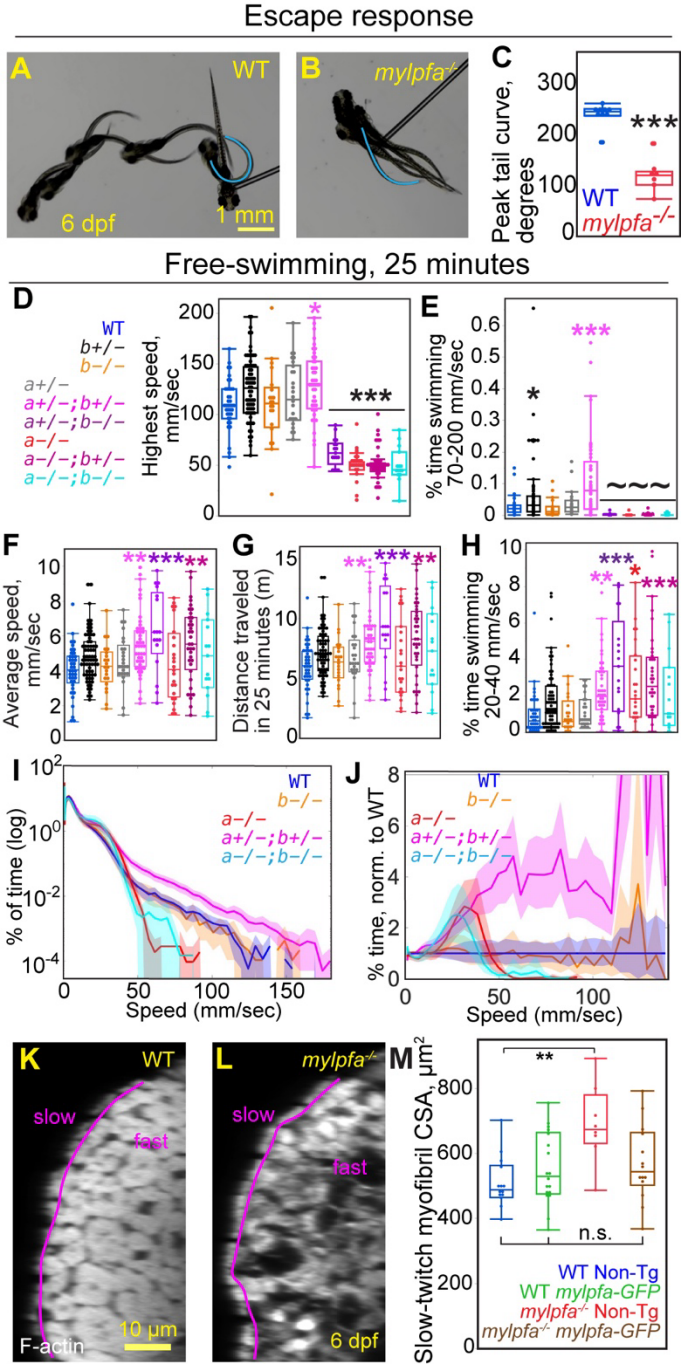

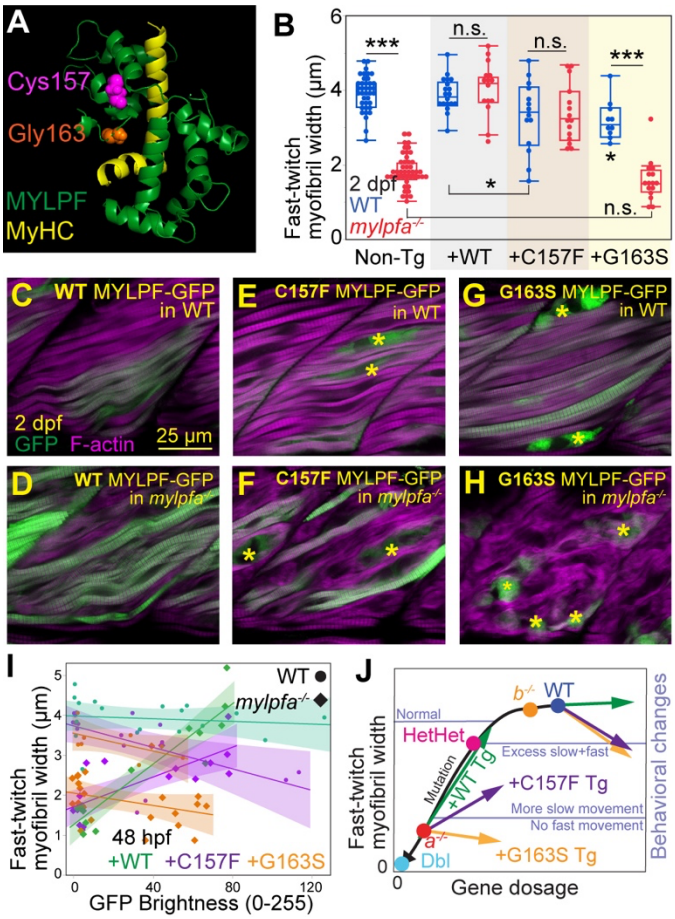

Figure 8: *MYLPF* alleles modeling variants in Distal Arthrogryposis patients do not promote early myofibril assembly. **(A)** Predicted MYLPF structure, with color and filled space highlighting the location of Cys157 and Gly163. **(B)** Box plots of myofibril widths in animals mosaic for the human MYLPF variants; the non-Tg group represents the compiled non-transgenic fibers from these animals. **(C-H)** Representative images of animals with mosaic expression of Mylpf transgenic variants (green), co-labeled for phalloidin (magenta) after fixation at 48 hpf. Animals are injected with the constructs *mylpfa:MYLPF-GFP,* expressing the WT MYLPF variant (C, D), C157F variant (E, F), and G163S variant(G, H). Areas with delocalized GFP are marked with an asterisk. **(I)** Scatterplot showing correlates between myofibril width and GFP brightness for all constructs injected. The R^2 values in the *mylpfa*$^{-/-}$ mutants are 0.86 (WT Tg), 0.55 (C157F), and 0.11 (G163S). In the WT siblings, R2 values are 0.02 (WT Tg), 0.36 (C157F), and 0.36 (G163S). **(J)** Model of how gene dosage impacts myofibril formation and fish behaviors during zebrafish embryonic development. Significance determined by Tukey-Kramer HSD comparisons after ANOVA: n.s. is P>0.1, * indicates P<0.05, *** indicates P<0.001. Scalebar in C is for C-H.

Supplemental Figures and legends

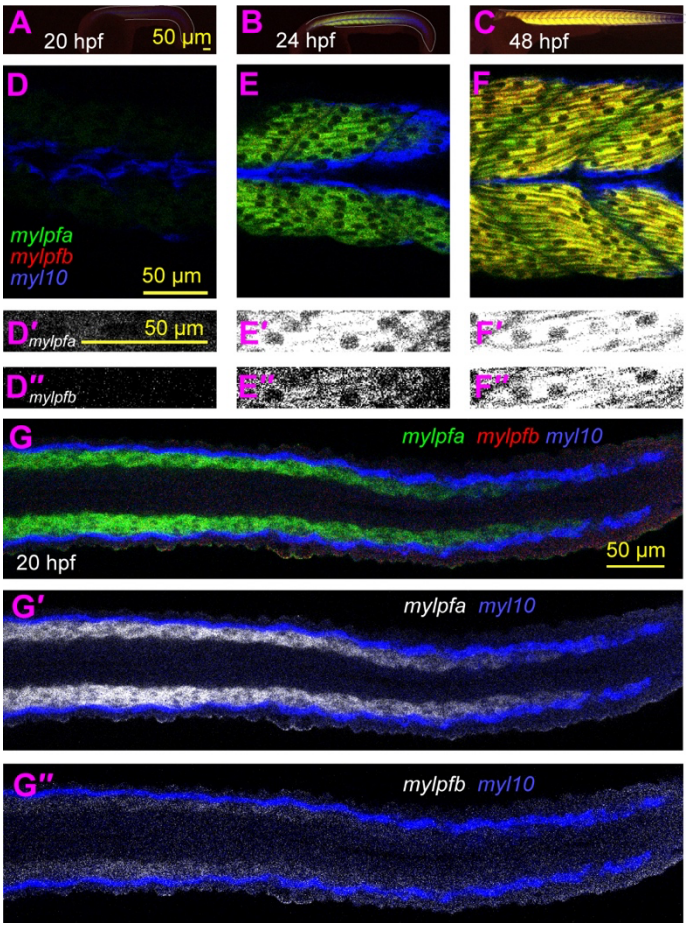

Figure S1: Time-course of *mylpfa* and *mylpfb* expression in fast-twitch muscle fibers. Images of HCR ISH for *mylpfa*, *mylpfb*, and the slow muscle marker *myl10.* **(A-C)** Low magnification images highlight that all three genes are expressed specifically in muscle and not in other body locations like the head. **(D-F″)** Confocal slices at higher magnification show that the two Mylpf genes are consistently excluded from slow-twitch fibers, but overlap in all fast-twitch fibers. Both genes are visible in the brightened single-channel inset at the stages examined (D′-F″). The ratio of *mylpfa* to *mylpfb* is somewhat lower in these co-labeled images (detected in 488 and 568 excitation) than in the single-channel ones shown in Figure 1G, H (detected in 488 channel), because of differential sensitivities between 488 and 568 detectors. **(G-G″)** Z-slice from a 20 hpf embryo shown from a transverse view, shown as a 3-color merge (G), merge of *myl10* and *mylpfa* (G**″**), and as a merge of *myl10* and *mylpfb* channels (G″). Both genes are present in fast-twitch myofibers, which are medial to slow twitch fibers by 20 hpf. Scalebar in A is for A-C, D is for D-F, D′ is for D′-F″, and G is for G-G″. Image settings are matched in A-C, D-F, and D′-F′ to allow comparisons between timepoints.

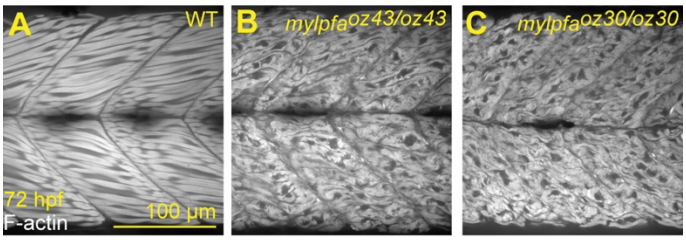

Figure S2: The *mylpfa*^{oz30} phenotypes are consistent with those found in the *mylpfa*^{oz43} mutant. **(A-C)** Confocal slices through the fast-twitch region of somites labeled for phalloidin at 72 hpf. Compared to wild-type siblings (A), myofibrils are disarrayed in the *mylpfa*^{oz30} mutant (B) and the *mylpfa*^{oz43} mutant (C). Scale bar in A applies to A-C.

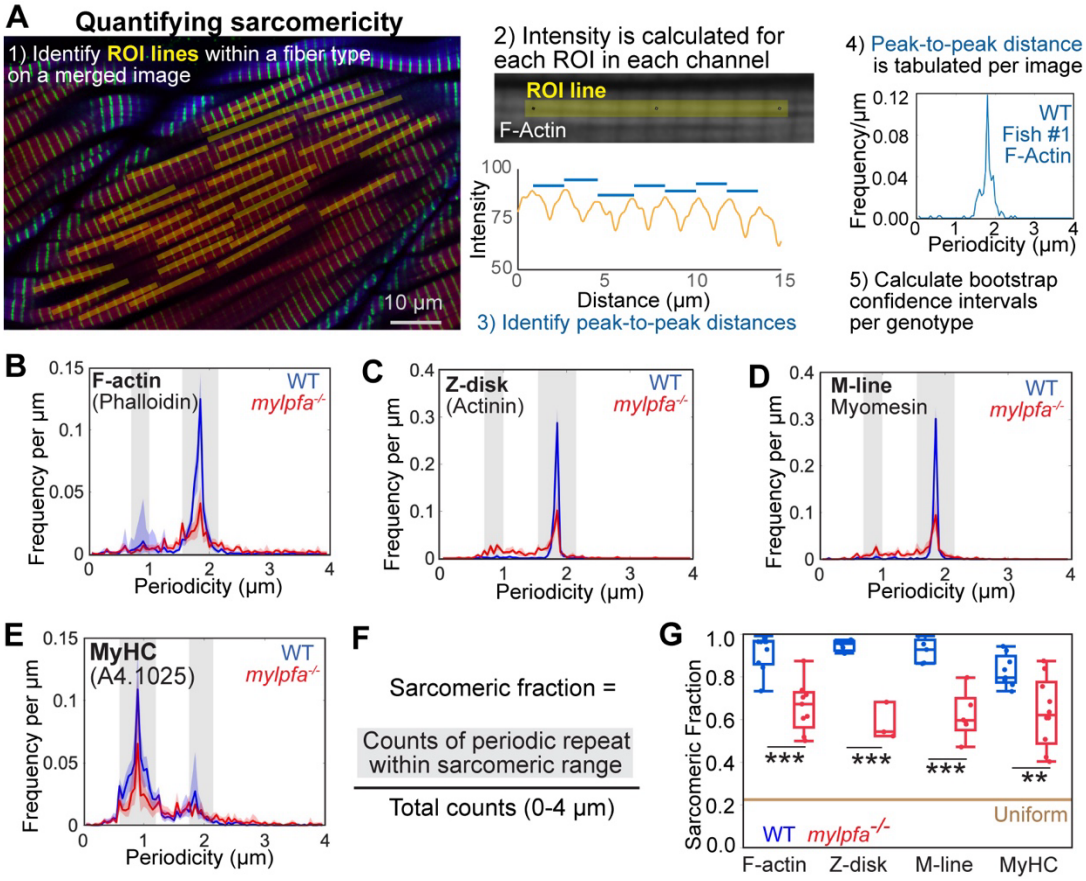

Figure S3: Explanation of the sarcomeric fraction calculation. **(A)** Overview of a method to quantify the degree to which markers localize to sarcomeres. 1) ROI lines are drawn throughout the fast-twitch muscle region of a dorsal somite half, with lengths of approximately 15 µm each. 2) An ImageJ script separates channels and calculates grayscale intensity across the ROI line shown on top of the F-actin channel. 3) The periodicity of each ROI is calculated, and repeats are binned by length. 4) Histogram plot of all ROI in one image, here binned to step size 0.05 µm, with peak frequency near the sarcomere length of 1.85 µm. 5) Each 0.05 µm histogram bin is averaged per image, then bootstrap confidence intervals are calculated using variation between images. **(B-E)** Histograms showing the frequency of periodicity in images. Colored lines represent mean values per genotype, semi-transparent colored lines indicate bootstrap confidence intervals, and gray bars indicating the sarcomeric intervals per marker. **(F)** Formula for calculating sarcomeric fraction, which is the ratio of signal in sarcomeric lengths (gray bars) to total localization (Y-axis, 0-4 µm) is the sarcomeric fraction. **(G)** Sarcomeric fractions are shown for F-actin (phalloidin), Z-disk (Actinin), M-line (Myomesin), and MyHC (A4.1025) labels. A horizontal brown line shows the fraction predicted by a uniform distribution. Data in S3B and S3G are replicated in main-text Figures 2K and 2L respectively. For all bar graphs and histogram plots, wild-type data is blue, and the *mylpfa*$^{-/-}$ mutant data is red. Significance thresholds were determined by Tukey-Kramer HSD comparisons; ** P<0.01, *** P<0.001.

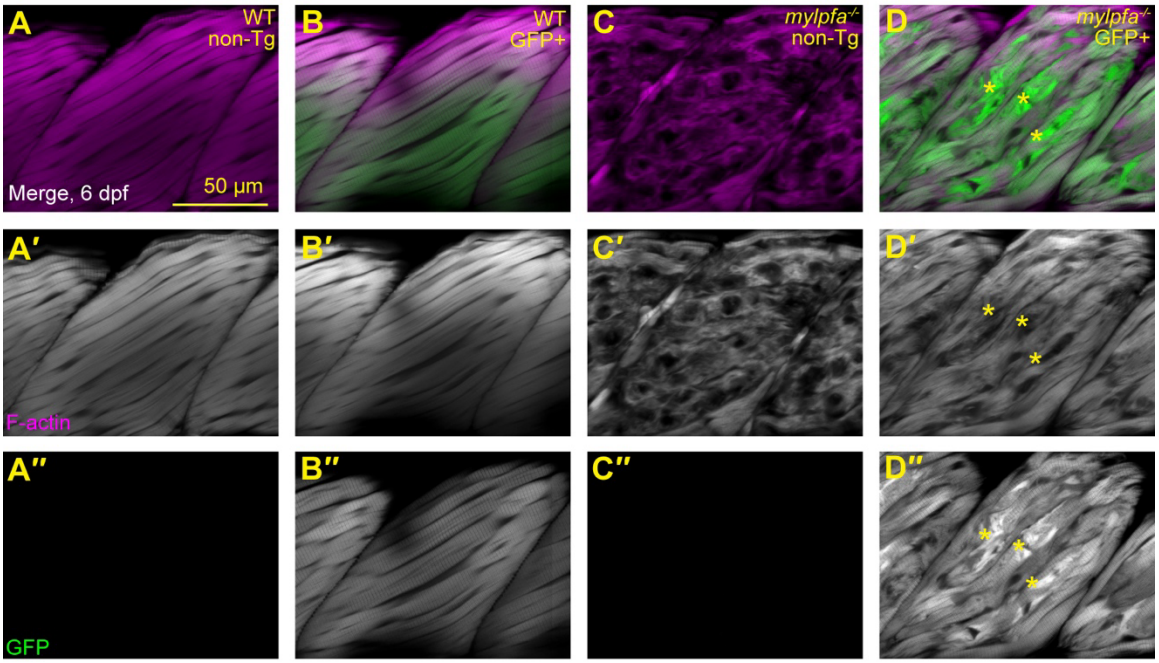

Figure S4: Representative examples of the *mylpfa-GFP* rescue experiments at 6 dpf. **(A-D″)** Confocal slices in sagittal view showing the dorsal half of somites. Images are shown as an overlay of phalloidin and GFP channels (A-D), as single channel for phalloidin (A′-D′), or as single channel for GFP (A″-D″),. At this stage we sometimes find patches of disordered GFP and Actin in the *mylpfa*$^{-/-}$ mutant at 6 dpf (asterisks) alongside the well-ordered myofibrils. Scalebar in A applies to all panels.

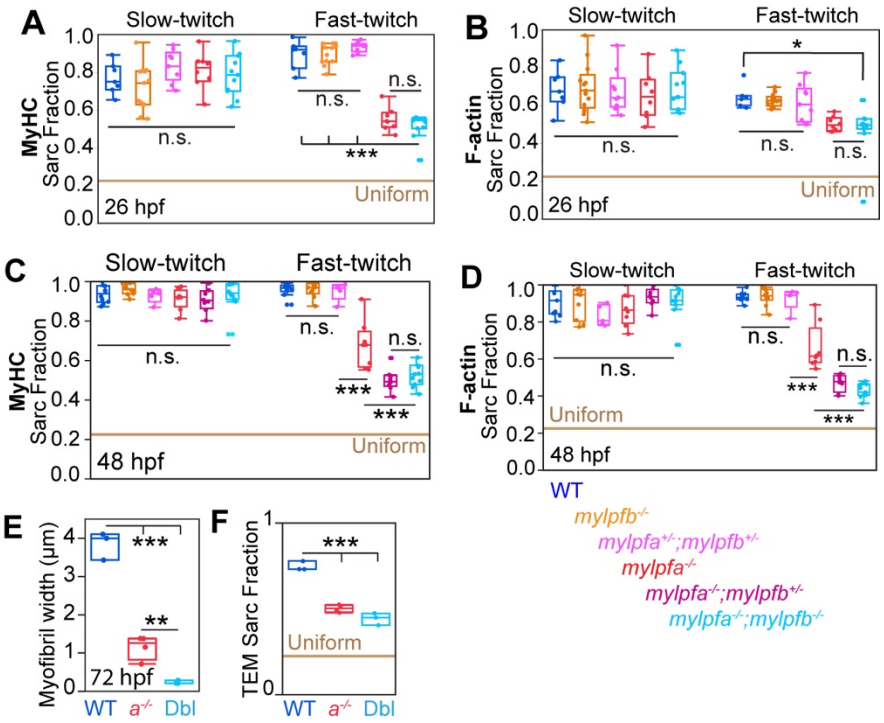

Figure S5: Comparison of muscle phenotypes in the *mylpfa*$^{-/-}$;*mylpfb*$^{-/-}$ incross through embryonic development. **(A)** Box plots showing the fraction of sarcomeric MyHC at 26hpf, **(B)** F-actin at 26 hpf, **(C)** MyHC at 48 hpf, and **(D)** F-actin at 48 hpf. Although F-actin localizes first, its periodicity increases later than MyHC so the shifts in the mutant are smaller for that gene in the earlier timepoint. The 48 hpf MyHC data is also shown in main text (Figure 5K); shown here for comparison with other datasets. The mutant's reduction in myofibril width and loss of sarcomeres persists to 72 hpf as seen in measurements of **(E)** myofibril width and **(F)** fraction of sarcomere-length objects in TEM. Genotypic color codes are shown in the figure. Significance thresholds were determined by Tukey-Kramer HSD comparisons (K); not significant (n.s.) is P>0.1, ** P<0.01, *** P<0.001.

Video 1: The *mylpfa*$^{-/-}$ mutant shows an impaired escape response. Imaging at 240 frames/second, showing 100 msec after contact with fishing line in the wild-type and the *mylpfa*$^{-/-}$ mutant. Both animals respond to the prodding; however, the *mylpfa*$^{-/-}$ mutant escapes at slower speed due to smaller tail undulations. Figure 7A, B shows a projection of frames from this video.

Tables:

n/a

Citations

1. Luis, N. M. & Schnorrer, F. Mechanobiology of muscle and myofibril morphogenesis. *Cells & Development* **168**, 203760 (2021).
2. Berger, J., Berger, S. & Currie, P. D. Mob4-dependent STRIPAK involves the chaperonin TRiC to coordinate myofibril and microtubule network growth. *PLoS Genet* **18**, e1010287 (2022).
3. Sanger, J. W. *et al.* Assembly and Maintenance of Myofibrils in Striated Muscle. in *The Actin Cytoskeleton* (ed. Jockusch, B. M.) vol. 235 39–75 (Springer International Publishing, Cham, 2016).
4. Holtzer, H. *et al.* Independent assembly of 1.6 microns long bipolar MHC filaments and I-Z-I bodies. *Cell Struct Funct* **22**, 83–93 (1997).
5. Rhee, D., Sanger, J. M. & Sanger, J. W. The premyofibril: Evidence for its role in myofibrillogenesis. *Cell Motility* **28**, 1–24 (1994).
6. Raeker, M. Ö., Shavit, J. A., Dowling, J. J., Michele, D. E. & Russell, M. W. Membrane-myofibril cross-talk in myofibrillogenesis and in muscular dystrophy pathogenesis: lessons from the zebrafish. *Frontiers in Physiology* **5**, (2014).
7. Weitkunat, M., Brasse, M., Bausch, A. R. & Schnorrer, F. Mechanical tension and spontaneous muscle twitching precede the formation of cross-striated muscle *in vivo*. *Development* **144**, 1261–1272 (2017).
8. Tskhovrebova, L. & Trinick, J. Titin and Nebulin in Thick and Thin Filament Length Regulation. in *Fibrous Proteins: Structures and Mechanisms* (eds. Parry, D. A. D. & Squire, J. M.) vol. 82 285–318 (Springer International Publishing, Cham, 2017).

9. Loison, O. *et al.* Polarization-resolved microscopy reveals a muscle myosin motor-independent mechanism of molecular actin ordering during sarcomere maturation. *PLOS Biology* **16**, e2004718 (2018).
10. Lemke, S. B. & Schnorrer, F. Mechanical forces during muscle development. *Mechanisms of Development* **144**, 92–101 (2017).
11. Hall, T. E. *et al.* In vivo cell biological screening identifies an endocytic capture mechanism for T-tubule formation. *Nat Commun* **11**, 3711 (2020).
12. Lowey, S. & Trybus, K. M. Role of Skeletal and Smooth Muscle Myosin Light Chains. *Biophysical Journal* **68**, 7 (1995).
13. Heissler, S. M. & Sellers, J. R. Myosin light chains: Teaching old dogs new tricks. *BioArchitecture* **4**, 169–188 (2014).
14. Sherwood, J. J., Waller, G. S., Warshaw, D. M. & Lowey, S. A point mutation in the regulatory light chain reduces the step size of skeletal muscle myosin. *Proceedings of the National Academy of Sciences* **101**, 10973–10978 (2004).
15. VanBuren, P. *et al.* The essential light chain is required for full force production by skeletal muscle myosin. *Proceedings of the National Academy of Sciences* **91**, 12403–12407 (1994).
16. Pastra-Landis, S. C. & Lowey, S. Myosin subunit interactions. Properties of the 19,000-dalton light chain-deficient myosin. *J. Biol. Chem.* **261**, 14811–14816 (1986).
17. Warmke, J., Yamakawa, M., Molloy, J., Falkenthal, S. & Maughan, D. Myosin light chain-2 mutation affects flight, wing beat frequency, and indirect flight muscle contraction kinetics in Drosophila. *The Journal of cell biology* **119**, 1523–1539 (1992).

18. Ravenscroft, G. *et al.* Bi-allelic mutations in MYL1 cause a severe congenital myopathy. *Human Molecular Genetics* (2018) doi:10.1093/hmg/ddy320.

19. Nawrotzki, R., Fischman, D. A. & Mikawa, T. Antisense suppression of skeletal muscle myosin light chain-1 biosynthesis impairs myofibrillogenesis in cultured myotubes. *J Muscle Res Cell Motil* **16**, 45–56 (1995).

20. Lossie, J. *et al.* Mutations of ventricular essential myosin light chain disturb myosin binding and sarcomeric sorting. *Cardiovascular Research* **93**, 390–396 (2012).

21. Cao, J. *et al.* The single-cell transcriptional landscape of mammalian organogenesis. *Nature* **566**, 496–502 (2019).

22. Wang, Y. *et al.* Fast skeletal muscle regulatory light chain is required for fast and slow skeletal muscle development. *The FASEB Journal* **21**, 2205–2214 (2007).

23. Hall, J. G. Arthrogryposis (multiple congenital contractures): Diagnostic approach to etiology, classification, genetics, and general principles. *European Journal of Medical Genetics* **57**, 464–472 (2014).

24. Bamshad, M., Van Heest, A. E. & Pleasure, D. Arthrogryposis: A Review and Update: *The Journal of Bone and Joint Surgery-American Volume* **91**, 40–46 (2009).

25. Whittle, J., Johnson, A., Dobbs, M. B. & Gurnett, C. A. Models of Distal Arthrogryposis and Lethal Congenital Contracture Syndrome. *Genes* **12**, 943 (2021).

26. Devoto, S. H., Melançon, E., Eisen, J. S. & Westerfield, M. Identification of separate slow and fast muscle precursor cells in vivo, prior to somite formation. *Development* **122**, 3371–3380 (1996).

1088 27. Mead, A. F., Kennedy, G. G., Palmer, B. M., Ebert, A. M. & Warshaw, D. M. Mechanical
1089 Characteristics of Ultrafast Zebrafish Larval Swimming Muscles. *Biophysical Journal* **119**,
1090 806–820 (2020).
1091 28. Talbot, J. & Maves, L. Skeletal muscle fiber type: using insights from muscle developmental
1092 biology to dissect targets for susceptibility and resistance to muscle disease. *Wiley*
1093 *Interdiscip Rev Dev Biol* **5**, 518–534 (2016).
1094 29. Roy, S. D. *et al.* Myotome adaptability confers developmental robustness to somitic
1095 myogenesis in response to fibre number alteration. *Developmental Biology* **431**, 321–335
1096 (2017).
1097 30. Farnsworth, D. R., Saunders, L. M. & Miller, A. C. A single-cell transcriptome atlas for
1098 zebrafish development. *Developmental Biology* **459**, 100–108 (2020).
1099 31. Sur, A. *et al.* Single-cell analysis of shared signatures and transcriptional diversity during
1100 zebrafish development. *Developmental Cell* S1534580723005774 (2023)
1101 doi:10.1016/j.devcel.2023.11.001.
1102 32. Thisse, B. *et al.* Spatial and temporal expression of the zebrafish genome by large-scale in
1103 situ hybridization screening. *Methods Cell Biol* **77**, 505–519 (2004).
1104 33. Xu, Y., He, J., Wang, X., Lim, T. M. & Gong, Z. Asynchronous activation of 10 muscle-specific
1105 protein (MSP) genes during zebrafish somitogenesis. *Developmental Dynamics* **219**, 201–
1106 215 (2000).
1107 34. Nassar, L. R. *et al.* The UCSC Genome Browser database: 2023 update. *Nucleic Acids Res* **51**,
1108 D1188–D1195 (2023).

35. Chong, J. X. *et al.* Mutations in MYLPF Cause a Novel Segmental Amyoplasia that Manifests as Distal Arthrogryposis. *The American Journal of Human Genetics* **107**, 293–310 (2020).

36. Ju, B. *et al.* Recapitulation of fast skeletal muscle development in zebrafish by transgenic expression of GFP under the mylz2 promoter. *Developmental Dynamics* **227**, 14–26 (2003).

37. Jackson, H. E. *et al.* The role of Sox6 in zebrafish muscle fiber type specification. *Skeletal Muscle* **5**, 2 (2015).

38. Gangras, P. *et al.* Zebrafish rbm8a and magoh mutants reveal EJC developmental functions and new 3'UTR intron-containing NMD targets. *PLoS Genet* **16**, e1008830 (2020).

39. Roberts, J. A. *et al.* Targeted transgene integration overcomes variability of position effects in zebrafish. *Development* **141**, 715–724 (2014).

40. Karuppasamy, M. *et al.* Standardization of zebrafish drug testing parameters for muscle diseases. *Disease Models & Mechanisms* **17**, dmm050339 (2024).

41. Bernick, E. P., Zhang, P.-J. & Du, S. Knockdown and overexpression of Unc-45b result in defective myofibril organization in skeletal muscles of zebrafish embryos. *BMC Cell Biology* **11**, 70 (2010).

42. Burghardt, T. P., Sun, X., Wang, Y. & Ajtai, K. In vitro and in vivo single myosin step-sizes in striated muscle. *Journal of Muscle Research and Cell Motility* **36**, 463–477 (2015).

43. Zhao, S. *et al.* Myosin-18B Promotes Mechanosensitive CaMKK2-AMPK-VASP Regulation of Contractile Actin Stress Fibers. *iScience* **23**, (2020).

44. Berger, J., Berger, S., Li, M. & Currie, P. D. Myo18b is essential for sarcomere assembly in fast skeletal muscle. *Human molecular genetics* **26**, 1146–1156 (2017).

45. Gurung, R. *et al.* A Zebrafish Model for a Human Myopathy Associated with Mutation of the Unconventional Myosin MYO18B. *Genetics* **205**, 725–735 (2017).

46. Okamoto, H. *et al.* Molecular characterization of mutant actin genes which induce heat-shock proteins in *Drosophila* flight muscles. *The EMBO Journal* **5**, 589–596 (1986).

47. Whittle, J. *et al.* MYH3-associated distal arthrogryposis zebrafish model is normalized with para-aminoblebbistatin. *EMBO Mol Med* e12356 (2020) doi:10.15252/emmm.202012356.

48. Zempo, B., Yamamoto, Y., Williams, T. & Ono, F. Synaptic silencing of fast muscle is compensated by rewired innervation of slow muscle. *Sci. Adv.* **6**, eaax8382 (2020).

49. Naganawa, Y. & Hirata, H. Developmental transition of touch response from slow muscle-mediated coilings to fast muscle-mediated burst swimming in zebrafish. *Developmental Biology* **355**, 194–204 (2011).

50. Lobjois, V. *et al.* A muscle transcriptome analysis identifies positional candidate genes for a complex trait in pig. *Animal Genetics* **39**, 147–162 (2008).

51. Ryan, M. T. *et al.* Polymorphisms in the regulatory region of the porcine MYLPF gene are related to meat quality traits in the Large White breed. *Meat Science* **113**, 104–106 (2016).

52. Zhang, R. *et al.* The Expression Profiles of mRNAs and lncRNAs in Buffalo Muscle Stem Cells Driving Myogenic Differentiation. *Frontiers in Genetics* **12**, (2021).

53. Aoki, H., Sadoshima, J. & Izumo, S. Myosin light chain kinase mediates sarcomere organization during cardiac hypertrophy in vitro. *Nat Med* **6**, 183–188 (2000).

54. Westerfield, M. *The Zebrafish Book: A Guide for the Laboratory Use of Zebrafish (Danio Rerio).* (University of Oregon Press, Eugene, 2007).

55. Kimmel, C. B., Ballard, W. W., Kimmel, S. R., Ullmann, B. & Schilling, T. F. Stages of embryonic development of the zebrafish. *Developmental dynamics* **203**, 253–310 (1995).

56. Talbot, J. C. & Amacher, S. L. A streamlined CRISPR pipeline to reliably generate zebrafish frameshifting alleles. *Zebrafish* **11**, 583–585 (2014).

57. Kawakami, K. Transgenesis and Gene Trap Methods in Zebrafish by Using the Tol2 Transposable Element. in *Methods in Cell Biology* vol. 77 201–222 (Academic Press, 2004).

58. Ignatius, M. S. *et al.* In vivo imaging of tumor-propagating cells, regional tumor heterogeneity, and dynamic cell movements in embryonal rhabdomyosarcoma. *Cancer Cell* **21**, 680–693 (2012).

59. Kwan, K. M. *et al.* The Tol2kit: a multisite gateway-based construction kit for Tol2 transposon transgenesis constructs. *Dev Dyn* **236**, 3088–3099 (2007).

60. Suster, M. L., Abe, G., Schouw, A. & Kawakami, K. Transposon-mediated BAC transgenesis in zebrafish. *Nature Protocols* **6**, 1998–2021 (2011).

61. Bird, N. C., Windner, S. E. & Devoto, S. H. Immunocytochemistry to Study Myogenesis in Zebrafish. in *Myogenesis* (ed. DiMario, J. X.) vol. 798 153–169 (Humana Press, Totowa, NJ, 2012).

62. Talbot, J. C., Johnson, S. L. & Kimmel, C. B. hand2 and Dlx genes specify dorsal, intermediate and ventral domains within zebrafish pharyngeal arches. *Development* **137**, 2507–2517 (2010).

63. Berberoglu, M. A. *et al.* Satellite-like cells contribute to pax7 -dependent skeletal muscle repair in adult zebrafish. *Developmental Biology* **424**, 162–180 (2017).

64. Grove, B. K. *et al.* A new 185,000-dalton skeletal muscle protein detected by monoclonal antibodies. *J Cell Biol* **98**, 518–524 (1984).

65. Webster, C., Silberstein, L., Hays, A. P. & Blau, H. M. Fast muscle fibers are preferentially affected in Duchenne muscular dystrophy. *Cell* **52**, 503–513 (1988).

66. Choi, H. M. T., Schwarzkopf, M. & Pierce, N. A. Multiplexed Quantitative In Situ Hybridization with Subcellular or Single-Molecule Resolution Within Whole-Mount Vertebrate Embryos: qHCR and dHCR Imaging (v3.0). in *In Situ Hybridization Protocols* (eds. Nielsen, B. S. & Jones, J.) 159–178 (Springer US, New York, NY, 2020). doi:10.1007/978-1-0716-0623-0_10.

67. Gulbulak, U., Wellette-Hunsucker, A. G., Kampourakis, T. & Campbell, K. S. GelBox: Open-source software to improve rigor and reproducibility when analyzing gels and immunoblots. *American Journal of Physiology-Heart and Circulatory Physiology* (2024) doi:10.1152/ajpheart.00144.2024.

68. Schindelin, J. *et al.* Fiji: an open-source platform for biological-image analysis. *Nat Methods* **9**, 676–682 (2012).

69. Baek, M. *et al.* Accurate prediction of protein structures and interactions using a three-track neural network. *Science* **373**, 871–876 (2021).

70. Mary, H. & Brouhard, G. J. *Kappa (κ): Analysis of Curvature in Biological Image Data Using B-Splines*. http://biorxiv.org/lookup/doi/10.1101/852772 (2019) doi:10.1101/852772.